Manuscript prepared for Atmos. Chem. Phys.
with version 5.0 of the LaTeX class copernicus.cls.
Date: 20 November 2014

Global investigation of the Mg atom and ion layers using SCIAMACHY/Envisat observations between 70 and 150 km altitude and WACCM-Mg model results

M. P. Langowski[1,2], C. von Savigny[2], J. P. Burrows[1], W. Feng[3,4], J. M. C. Plane[3], D. R. Marsh[5], D. Janches[6], M. Sinnhuber[7], A. C. Aikin[8], and P. Liebing[1]

[1]Institute of Environmental Physics (IUP), University of Bremen, Germany
[2]Institut für Physik, Ernst-Moritz-Arndt-Universität Greifswald, Germany
[3]School of Chemistry, University of Leeds, UK
[4]National Centre for Atmospheric Science, University of Leeds, UK
[5]National Center for Atmospheric Research, Boulder, Colorado, USA
[6]Space Weather Lab, GSFC/NASA, USA
[7]Institut für Meteorologie und Klimaforschung – Atmosphärische Spurengase und Fernerkundung, KIT, Karlsruhe, Germany
[8]The Catholic University of America, Washington D.C., USA

Correspondence to: M. Langowski (langowskim@uni-greifswald.de)

Abstract. Mg and Mg^+ concentration fields in the upper mesosphere/lower thermosphere (UMLT) region are retrieved from SCIAMACHY/Envisat limb measurements of Mg and Mg^+ dayglow emissions using a 2-D tomographic retrieval approach. The time series of monthly mean Mg and Mg^+ number density and vertical column density in different latitudinal regions are presented. Data from the limb mesosphere-thermosphere mode of SCIAMACHY/Envisat are used, which covers the 50 to 150 km altitude region with a vertical sampling of ≈ 3.3 km and latitudes up to 82°. The high latitudes are not observed in the winter months, because there is no dayglow emission during polar night. The measurements were performed every 14 days from mid-2008 until April 2012. Mg profiles show a peak at around 90 km altitude with a density between 750 cm^{-3} and 1500 cm^{-3}. Mg does not show strong seasonal variation at latitudes below 40°. For higher latitudes the densities are lower and only in the northern hemisphere a seasonal cycle with a summer minimum is observed. The Mg^+ peak occurs 5–15 km above the neutral Mg peak altitude. These ions have a significant seasonal cycle with a summer maximum in both hemispheres at mid and high latitudes. The strongest seasonal variations of Mg^+ are observed at latitudes between 20–40° and densities at the peak altitude range from 500 cm^{-3} to 4000 cm^{-3}. The peak altitude of the ions shows a latitudinal dependence with a maximum at mid latitudes that is up to 10 km higher than the peak altitude at the equator.

The SCIAMACHY measurements are compared to other measurements and WACCM model results. The WACCM results show a significant seasonal variability for Mg with a summer mini-

mum, which is more clearly pronounced than for SCIAMACHY, and globally higher peak densities than the SCIAMACHY results. Although the peak densities are not in agreement, the vertical column densities agree well, because SCIAMACHY and WACCM profiles have different widths. The agreement between SCIAMACHY and WACCM results is much better for Mg^+ with both showing the same seasonality and similar peak densities. However, there are also minor differences, e.g. WACCM showing a nearly constant altitude of the Mg^+ layer's peak density for all latitudes and seasons.

1 Introduction

The amount of meteoric mass deposited daily on the earth upper atmosphere is estimated to range from 2 to 300 tons (see, e.g. table 1 of Plane, 2012, and references therein, and Feng et al. (2013), Marsh et al. (2013a) and Gardner et al. (2014)).

Since the number of extraterrestrial particles encountering the Earth's atmosphere is approximately inversely proportional, in a log-log scale, to the particle's size, the bulk of the daily meteoric mass flux is contributed mainly by particles in the 1–100 micrometer (in radius) size range (Ceplecha et al., 1998; Flynn, 2002; Mathews et al., 2001; Nesvorný et al., 2010, 2011a,b). Furthermore, most of the daily mass input originates from the sporadic meteor background, which is the interplanetary dust forming the Zodiacal dust cloud. The orbits of the meteoroids from that source are so evolved that they cannot be traced back to their original parent body (Brown and Jones, 1995; Janches et al., 2006; Fentzke and Janches, 2008). The constant bombardment of particles from the sporadic background contributes far more input than meteor showers (e.g. Murad and Williams, 2002), the latter being a time-limited (days to several weeks) enhancement of particles entering the atmosphere in parallel trajectories appearing to radiate from one point in the sky (Jenniskens, 2006).

When meteoroids enter the atmosphere at geocentric speeds between 11 to 72 $\mathrm{km\,s^{-1}}$, they collide with air molecules, leading to frictional heating and deceleration. The meteoroids, consisting partly of metals, melt at their surfaces and metals are ablated. The ablation process depends on several factors, such as the entry velocity and angle of the meteoroid, the boiling point of the different constituents and the size of the meteoroid (see, e.g. McNeil et al. (1998) and Vondrak et al. (2008) for more details). For the micron-size particles of interest to this work, the ablation process occurs between 80 and 125 km (Vondrak et al., 2008; Janches et al., 2009; Marsh et al., 2013a; Feng et al., 2013; Plane et al., 2014), resulting in the deposition of metallic atoms such as sodium (Na), iron (Fe), potassium (K) and magnesium (Mg) in the Mesosphere and Lower Thermosphere (MLT).

The observation technique, used in this study, measures the number density of the metal atom and ion layers present in the MLT that are formed from the ablated material from the meteoroids. Once ablated the meteoric metals undergo chemical transformation (see, e.g. Plane, 2003). A fraction of the ablated metals in the ablation region (80 to 105 km) is already in the ionized form. For the case

of Mg^+ this fraction is estimated to be negligibly small (Vondrak et al., 2008, Fig. 14.). Mg^+ is formed by charge exchange of Mg with the main ion constituents at this altitude, i.e. NO^+ and O_2^+. The dominant loss process for Mg is the reaction with O_3, which leads to stable oxides, hydroxides and carbonates as reservoir species. Mg^+ is lost by reactions with O_3 but also by reactions with N_2 and other trace gases (CO_2, H_2O) (see, e.g. Fig. 9 in Plane and Whalley (2012) for a schematic diagram of the most important reactions).

The metal molecules condense and form meteoric smoke particles (e.g. Hunten et al., 1980; Kalashnikova et al., 2000; Saunders and Plane, 2006). These meteoric smoke particles are thought to act as nucleation nuclei. Heterogeneous nucleation of clouds is thought to play an important role in the formation of noctilucent clouds (NLC) (see, e.g. Rapp and Thomas, 2006) in the polar summer mesopause region and also in the formation of polar stratospheric clouds (PSC) in the polar winter stratosphere (see, e.g. Voigt et al., 2005; Curtius et al., 2005). PSC have an important role in the ozone chemistry and the depletion of stratospheric ozone. In a dynamical equilibrium of meteoroid input and the above mentioned loss reactions, the neutral Mg layer is formed between 85 and 90 km altitude and the Mg^+ layer is formed slightly above the Mg layer (see, e.g. Plane and Helmer, 1995; McNeil et al., 1998 and Plane and Whalley, 2012).

The MLT is not readily probed by in-situ instrumentation, as balloons fly too low, and satellites have to fly higher because of the atmospheric drag that reduces the satellite's operation time. As a result, only rockets carrying in-situ instrumentation are able to access this region (see Sect. 6 for references). These are, however, expensive and rare. Metal atoms and ions have very strong absorption coefficients and oscillator strengths (see, e.g. Kramida et al., 2012). As a result, although their densities even in the peak region are only a few thousand particles per cubic centimeter at most (for Na, Fe, Mg, less for others), they are very strong emitters of resonance fluorescence.

Mg and Mg^+ spectral lines are observed at wavelengths below 290 nm. This wavelength region is strongly affected by ozone absorption in the stratosphere, so that observations from ground are not possible. For this reason the knowledge of the Mg and Mg^+ content in the MLT is poor.

In this study the dayglow emissions of Mg and Mg^+, detected by the satellite experiment SCIAMACHY (Scanning Imaging Absorption Spectrometer for Atmospheric CHartographY) on Envisat (Environmental Satellite) are used. The Mg and Mg^+ densities are retrieved by mathematical inversion of these measurements using a radiative transfer model. Mg and Mg^+ profiles had already been retrieved from SCIAMACHY by Scharringhausen et al. (2008a,b). As a result of these investigations a novel optimised measurement mode for the purpose of better covering the peak region of Mg and Mg^+ has been established, and the observations are used for this study.

The resulting new data products are compared in this study with other Mg and Mg^+ measurements, as well as with WACCM-Mg simulations. WACCM-Mg combines different models: a Meteor Input Function model is coupled to a meteor differential ablation model, which provides the metal input in the MLT. The metal release into the upper atmosphere is then used as one input

to simulations using the Whole Atmosphere Community Climate Model (WACCM) (Marsh et al., 2013b) including a new chemistry model of Mg and Mg^+ (Plane and Whalley, 2012). WACCM is a general circulation model that incorporates interactive chemistry for both neutral and ion species.

In Sects. 2 and 3 the SCIAMACHY/Envisat satellite observations and the Mg and Mg^+ density retrieval are briefly described. In Sects. 4 and 5 the results obtained for Mg and Mg^+ are presented and discussed. In Sect. 6 these findings are compared to other measurements. In Sect. 7 the WACCM-Mg model simulations of Mg and Mg^+ are introduced and the model simulations are compared with the SCIAMACHY dataset. In Sect. 8 a possible connection between Mg and Mg^+ results and NLC is discussed. Finally, Sect. 9 summarizes the results obtained in this study.

2 Instrument and algorithm

SCIAMACHY, a satellite-borne grating spectrometer on Envisat, was launched by ESA (European Space Agency) on 28 February 2002 (see, e.g. Burrows et al., 1995; Bovensmann et al., 1999). Envisat flies in a sun-synchronous orbit with a 10:00 a.m. descending node. The duration of one orbit is roughly 100 min (15 orbits per day). Note that the local time of SCIAMACHY limb observations changes with latitude. It is ≈ 11 a.m. at 60° N and 9 a.m. at 60° S and, as shown in Fig. 1, varies strongly in the vicinity of the poles. The highest latitude covered by SCIAMACHY limb observations of scattered light is $\approx 82^\circ$.

Data from SCIAMACHY's limb MLT-mode with tangent altitudes between ≈ 50 and $\approx 150\,\mathrm{km}$ covered in 30 consecutive $\approx 3.3\,\mathrm{km}$ steps are used in this study. Dependent on latitude, consecutive limb measurements have a latitudinal separation of up to 8°, because nadir measurements are performed between two MLT-measurements. However, there is also a small latitude offset between MLT measurements in two consecutive orbits, to improve the meridional sampling for zonal averages.

MLT-measurements were performed from mid 2008 until the loss of contact to Envisat in April 2012. They were performed roughly every two weeks for 15 consecutive orbits, which corresponds to one day of consecutive measurements. This means, that measurements on 84 single days were performed, which is roughly a quarter year of single day data. This is much less than 4 years of single day data, and there are no continuous daily observations in the MLT-mode. Apart from a few days, where some orbits are missing in the data, all longitudes are equally covered (sampling every 24° of longitude).

The two-dimensional retrieval algorithm uses all measurements of one orbit and retrieves the metal densities from each emission line of the species on a latitude and altitude grid. For averaged data, a reference orbit for geolocations is used, which is formed from the geolocations of the data that is averaged. Measurements with similar latitudes and local times as the measurements of the reference orbit are averaged. For Mg the spectral line at 285.2 nm is used. For Mg^+ the spectral lines at

279.6 nm and 280.4 nm are used. A comprehensive discussion of the algorithm was provided by Langowski et al. (2013). Langowski et al. (2013) also present an extensive discussion of systematic and statistical errors and, e.g. also explain why only data for altitudes above 70 km altitude is used in this study.

An improvement compared to the analysis described by Langowski et al. (2013) is achieved by correcting the measured spectra for the polarization response of the instrument. This is briefly discussed in Sect. 3. As the main focus of this study is on the results of the retrieval algorithm, this discussion is kept short and more details can be found in Langowski (2014).

The first measurements at the start of the sunlit part of each orbit (high/mid northern latitudes) are contaminated by solar stray-light, which can be seen in the dark signal measurement at 350 km tangent altitude. We therefore exclude these measurements and also adjacent measurements, for which the contamination can not be clearly excluded. When using the remaining measurements, some of the features similar to the ones resulting from this error source are still observed. However, these features are not dependent on the orbit phase like the ones resulting from the stray-light contamination, but only appear at latitudes $> 78^\circ$ N, and it is not clear whether these features are real or not (see discussion of Fig. 21 at the end of Sect. 7.2).

The actual latitude grid for calculating the densities has a larger extent than the shown results. This is because the outermost latitude intervals have been cut off to reduce edge effects, which may, however, affect the neighboring latitudes. In Sect. 8, where near polar effects are discussed less data is cut off.

3 Polarization correction

SCIAMACHY is sensitive to the polarization of the incoming radiation. This was known before launch and wavelength dependent correction parameters were measured. The majority of backscattered radiation from the Earth's atmosphere is produced by Rayleigh-scattering, which polarizes the incoming unpolarized solar radiation. The resonance fluorescence process of metals results in nonzero polarization of radiation even if the incoming beam is unpolarized, depending on the change of angular momentum between the electronic states that are involved in the fluorescence process. The polarization of the resonance fluorescence process from metals is well described by Hamilton (1947) and can also be found in Chandrasekhar (1960) with a slightly different nomenclature in the used formulas.

The incoming solar radiation is assumed to be unpolarized, which means that the parallel and perpendicular intensity components are equal in any observation plane. Following (Chandrasekhar, 1960, Eq. (259), page 51) the incoming radiation components parallel and perpendicular to the

scattering plane are transformed as follows:

$$\begin{pmatrix} I_{\parallel out} \\ I_{\perp out} \end{pmatrix} = \left(\frac{3}{2} E_1 \begin{pmatrix} cos^2\theta & 0 \\ 0 & 1 \end{pmatrix} + \frac{1}{2} E_2 \begin{pmatrix} 1 & 1 \\ 1 & 1 \end{pmatrix} \right) \begin{pmatrix} I_{\parallel in} \\ I_{\perp in} \end{pmatrix} \quad (1)$$

The parallel component is dependent on the scattering angle θ, which leads to nonzero polarization, if $E_1 \neq 0$. The parameters (E_1,E_2) are (1,0) for Mg at 285.2 nm, (0.5,0.5) for Mg^+ at 279.6 nm and (0,1) for Mg^+ at 280.4 nm. The coordinate system independent degree of polarization P is $\sqrt{\left(\frac{I_{\parallel out} - I_{\perp out}}{I_{\parallel out} + I_{\perp out}}\right)^2}$, and the polarization angle χ is perpendicular to the scattering plane.

The response of SCIAMACHY depends on the polarization state of the radiation, so that an accurate absolute calibration requires the effect to be corrected for. Until recently, this was not possible because the available set of calibration data for the polarization sensitivity which is provided with the Level 1 data suffered from severe errors, in particular for the limb measurement geometry and studies for an improvement of this effect in the calibration are still being done (see, e.g. Krijger et al. (2014) and Liebing et al. (2013)).

From in-flight data it is possible to derive polarization sensitivities in the wavelength range below 300 nm by comparing measured reflectances with the ones calculated by a vector radiative transfer model (SCIATRAN 3.1, see, e.g. Rozanov et. al. (2014)) and then fitting the differences to the expected polarization. The results of this fit have been applied here together with Eq. (1) and a transformation to the SCIAMACHY polarization reference frame.

To derive the polarization sensitivities an ozone profile has to be assumed. The error due to the unknown actual ozone distribution is estimated to be quite large. This is why a consistency check to this approach has been performed here. Assuming the unpolarized Mg^+ line at 280.4 nm (D_1 line) to yield exact results, a correction factor for the line at 279.6 nm (D_2 line) can then be determined requiring that the densities retrieved from both Mg^+ lines match. Assuming that the polarization sensitivity does not change between 280 and 285 nm wavelength, a correction factor for Mg can be calculated knowing that the degree of polarization P_{D_2} of the D_2 line is just half of the degree of polarization P_{Mg} of the Mg line.

In cases where the Mg^+ signal is not dominated by noise, the results from both methods agree with each other well for Mg. Similarly the Mg^+ densities from both lines retrieved using the updated polarization correction for SCIAMACHY are in good agreement. We therefore conclude that the polarization correction for the 280-285 nm region improved the calibration of the data considerably.

4 Seasonal variations of Mg

The seasonal variations of Mg and Mg^+ densities on a latitude and altitude grid are investigated. Prior to averaging, measurements at night or those having noise peaks in the investigated spectral region, caused by highly energetic particles hitting the detector (e.g. in the Southern Atlantic Anomaly region), are removed from the data set by filtering. The limb spectra of up to 15 daily single orbits

are zonally averaged before running the retrieval algorithm, to improve the signal to noise ratio. To further reduce the noise in the results, data for individual months are averaged for the entire measurement period.

The retrieval algorithm produces densities on an altitude and latitude grid with 40 equidistant day-side latitude intervals between $82°$ S and $82°$ N and 80 altitude intervals with $1\,\mathrm{km}$ thickness between 70 and $150\,\mathrm{km}$. Additionally, there are latitude intervals for the part of the orbit, where the satellite moves northwards (see Fig. 1), to overcome ambiguities of identical latitudes but different local time at high latitudes.

The monthly averaged results for Mg are shown in Fig. 2. Mg shows a peak at around $90\,\mathrm{km}$ with densities up to $1500\,\mathrm{cm}^{-3}$. There is a strong month-to-month variability in the latitudinal distribution. The annual mean results for Mg are shown in Fig. 3. In the annual mean, the densities at low latitudes are higher than at the high latitudes in the peak region. At the highest southern latitude covered there are increased densities above $100\,\mathrm{km}$, which, however, are most likely explained by the fact that at this latitude the number of measurements is smaller and the statistical error thus larger.

Figure 4 shows the seasonal variation of the vertical profile for low, mid and high latitudes, and Fig. 5 shows the vertical column densities (VCD). The month-to-month variations are large, and thus the error on the estimate of the amplitude of seasonal variations for mid latitudes is relatively large. The seasonal variation of the Mg peak altitude is estimated to be less than $5\,\mathrm{km}$.

The VCD of Mg varies between $0.5 \times 10^9\,\mathrm{cm}^{-2}$ and $3.5 \times 10^9\,\mathrm{cm}^{-2}$ and is around $1.75 - 2.5 \times 10^9\,\mathrm{cm}^{-2}$ for most latitudes and times. The VCD between 40° N and 40° S is higher than for higher latitudes, which are only covered in the hemispheric summer and show a summer minimum, which however is only clearly observed in the Northern Hemisphere. The seasonal variation is small compared to the mean of the vertical column densities. This relatively small variation is required to retrieve the correct mean value, because of non-linearities in the retrieval, as comprehensively discussed and explained by Langowski et al. (2013).

5 Seasonal variations of Mg^+

For Mg^+ the same approach for data averaging is used as described for Mg in Sect. 4. For Mg^+ there are two spectral lines, one at $279.6\,\mathrm{nm}$ and the other one at $280.4\,\mathrm{nm}$. Both emission lines yield very similar results and only the results for the $280.4\,\mathrm{nm}$ line are shown. This line is not affected by polarization related issues, but has the larger statistical error. Mg^+ densities are independently retrieved from both lines. The differences in the peak region are lower than $25\,\%$.

The densities on an altitude and latitude grid for the monthly averaged results are shown in Fig. 6. The Mg^+ densities peak at altitudes in the range of 95–105 km with peak values of 500–4000 cm^{-3}. The peak densities show a seasonal variation with a summer maximum between 25–$45°$ in both hemispheres. In summer the highest peak altitude is roughly at $45°$ (N and S). It occurs around

105 km, which is up to 10 km higher than the lowest peak altitude at the equator and higher than that at the high latitude region. There is a minimum at the equator and also a second maximum in peak altitude in the mid latitudes in the winter hemisphere, that, however, is more variable than the one in the summer hemisphere.

The latitudinal variation of Mg^+ is also seen in the average over all available measurements in 2008–2012, which is shown in Fig. 7. The latitudinal dependence of the peak altitude seems to be symmetric to the equator. However, there is an asymmetry in the peak density, with larger densities for the Northern Hemisphere (NH) than for the Southern Hemisphere (SH). However, this effect is compensated by a broader profile in the SH, so that the differences in the vertical column densities are smaller.

A reason for this may be Lorentz force induced transport processes together with the very different mapping of geomagnetic coordinates to geographic coordinates (the magnetic southpole at around 65° S is further away from the geographic pole than the magnetic northpole at around 82° N).

At the upper vertical profile edge up to 110 km the density is higher at mid latitudes than at the equator, which can be explained by the density maximum at mid latitudes being also at higher altitudes, than at the equator. However, above 110 km altitude this behaviour is reversed and the equatorial densities are larger than the densities at mid latitudes. This may be explained by enhanced vertical upward transport in the equatorial region, which will be discussed in Sect. 7.2.

Figure 8 shows the seasonal variation of the vertical Mg^+ profile for low, mid and high latitudes, and Fig. 9 shows the corresponding VCD. In each of the latitude regions, a maximum in peak altitude is found during summer in the corresponding hemisphere. The VCD varies between $1 \times 10^9\,cm^{-2}$ and $6 \times 10^9\,cm^{-2}$. A seasonal cycle with a summer maximum is observed and the strongest variations are observed at latitudes between 20° and 40°.

Figure 10 shows the ratio of Mg^+ and Mg VCD. The ratio is in between 0.5 and 5. The seasonal variability of the ratio follows the one of Mg^+, as Mg (beside for northern high latitudes) does not show a strong seasonal variability.

6 Comparison to other measurements

Mg and Mg^+ cannot be observed from the ground, because the wavelengths of the lines are below 300 nm and the emission signal is absorbed strongly by ozone in the stratosphere. As a result, only few measurements are available and rely on observations from sounding rockets and satellites. The first rocket-borne ion mass spectrometer measurement of metal ions was reported by Johnson and Meadows (1955) (May 1954, White Sands) and enhanced ion signals between 93 and 124 km were found. According to Grebowsky and Aikin (2002) approximately 50 flights of rocket-borne mass spectrometers had been made until 2002, probing the region between 80 and 130 km. Results of these flights for Mg^+ can, e.g. be found in Istomin (1963), Narcisi and Bailey (1965), Narcisi

(1971), Aikin and Goldberg (1973), Philbrick et al. (1973), Zbinden et al. (1975), Herrmann et al. (1978), Kopp and Herrmann (1984), Kopp et al. (1985b,a), Kopp (1997) and Roddy et al. (2004). Date, local time, latitude and reference publications of these and other rocket flights can also be found in table 1 of Grebowsky et al. (1998). Figure 11 shows reproduced plots of vertical number density profiles of Mg^+. The original sources of the data for these plots are listed in table 1.

A disadvantage for the comparison with the new dataset presented in this study is that most of these measurements were performed during special events having E_s layers (sporadic electron layers), aurora, meteor showers, stratospheric warmings or NLC present. Sporadic $\mathrm{Mg^+}$ layers often occured between 105–110 km and/or at around 120 km. The $\mathrm{Mg^+}$ peak altitude in most of these measurements can be found between 90 and 95 km altitude and the full width at half maximum (FWHM) of the layers is on the order of 5–10 km, but sometimes the FWHM is only 1 km.

When comparing in-situ mass spectrometer measurements with satellite remote sensing results, it has to be noted that the in-situ measurements are localized and limited to the direct vicinity of the rocket. In contrast, remote sensing techniques typically cover a large volume with horizontal distances along and perpendicular to the viewing direction of several hundreds of kilometers. This results in smoother layers with a larger FWHM for the remote sensing method. Still, the width of the $\mathrm{Mg^+}$ layers as well as the peak densities presented in this study are in good agreement with the in-situ rocket measurements. However, the strong latitudinal dependence of the peak altitude observed in Fig. 8 as retrieved from SCIAMACHY measurements is not found in the in-situ rocket data.

In addition to the in-situ measurements with rockets, there are also airglow measurements available from rockets, the space shuttle and satellites. However, to retrieve density information from this method radiative transfer models as well as inversion techniques and computational power is needed. As a result, slant column information rather than profiles has been retrieved and made available in the first remote sensing studies (see, e.g. Boksenberg and Gérard, 1973 or Gérard and Monfils, 1974). In Anderson and Barth (1971) (Summer, $\approx 40^\circ$ N) the region up to 106 km altitude is scanned during a sporadic E_s layer event, and the peak altitude of the $\mathrm{Mg^+}$ was not observed during this flight, i.e. it was higher than 106 km. No Mg signal above the instrumental noise was observed in these spectra.

The region above the peak altitude from 150 km up to the F-layer and above was investigated by Gérard and Monfils (1978), Fesen and Hays (1982a), Mende et al. (1985), Gardner et al. (1995) and Gardner et al. (1999) and typically shows less than 100 $\mathrm{cm^{-3}}$ $\mathrm{Mg^+}$ ions at 150 km altitude. This is in good agreement with the profiles described in Sect. 5. In some cases higher densities are observed in the profiles retrieved from the SCIAMACHY limb observations. These are explained by retrieval artifacts on the edge of the retrieval grid and vertical constraints tuned for the main peak. These effects result in small oscillations, compared to the main peak, in regions with lower densities. Since these artifacts appear at the upper edge of the profile it also implies that there is a significant density above the highest tangent altitude for $\mathrm{Mg^+}$.

In Minschwaner et al. (2007) a combined NO and Mg^+ retrieval for satellite limb measurements is shown, which is in good agreement with the results in Sect. 5 in terms of the Mg^+ concentrations at peak altitude and at the upper edge of the profile. However, the Mg^+ peak altitude is at 90 km. Taking into account the coarser sampling (every 7 km), higher statistical errors and a tangent height offset ($\pm$4 km) in Minschwaner et al. (2007), the agreement is reasonable. Accurate tangent height determination was an an issue for SCIAMACHY, too. Offsets of a similar magnitude were initially observed for SCIAMACHY data products (see, e.g., von Savigny et al., 2005). However, this error source was minimized and the tangent height knowledge was improved to $\pm$200 m (von Savigny et al., 2009). The NO band emission, which overlaps with the Mg^+ lines and the Mg line, is on the same order of magnitude as the Mg^+ lines in the study by Minschwaner et al. (2007) and even bigger than the Mg emission, which made a NO correction necessary. The SCIAMACHY MLT dataset does not show these strong NO lines at 280 and 285 nm. NO in this region is very sensitive to solar activity. Results on NO retrievals from the same SCIAMACHY level 1 dataset as used in this study are reported by Bender et al. (2013). Only at high latitudes in summer and winter and from late 2011 to 2012 the results of Bender et al. (2013) show NO densities of the same magnitude as the equatorial density plot for NO in Minschwaner et al. (2007). However, we did not observe clear NO signals in the vicinity of the Mg/Mg^+ lines during this period.

A time series of Mg^+ vertical columns covering several years and retrieved from SBUV nadir measurements was presented by Joiner and Aikin (1996). These measurements were performed approximately 1 day per month, with a spectral resolution of 1.13 nm and a spectral sampling every 0.2 nm (compare to SCIAMACHY with $\approx$0.22 nm resolution and sampling every $\approx$0.11 nm). The results in Joiner and Aikin (1996) are in very good agreement with the results obtained in this study, especially when comparing Figs. 10 and 11 in Joiner and Aikin (1996) with Fig. 9 in this study. Figs. 12 and 13 show redrawn VCD timeseries from different sources for a quick and easy comparison of the results of Mg^+ and Mg (Please see the original sources for more details).

Mg was also investigated in Joiner and Aikin (1996). However, the average VCD for these profiles, where the signal was significant, is $4 \times 10^{10}\,cm^{-2}$, which is a factor of 10 more than the VCD in Fig. 5. These large discrepancies must be investigated in the future.

Satellite measurements with long time series and daily coverage are available from GOME and GOME-2 in nadir mode and from SCIAMACHY in nadir and nominal limb mode. All 3 instruments have a similar spectral resolution. VCD of Mg and Mg^+ were retrieved from the GOME dataset by Correira et al. (2008, 2010) and Correira (2009). Figures 1 and 2 in Correira et al. (2008) show Mg and Mg^+ VCD for 1996 and 1997 as well as the Mg^+ to Mg ratio for latitude intervals from 0–10° and 30–40° for both hemispheres. For the low latitudes, where there is less seasonality the VCD for Mg^+ are about 6–7$\times 10^9\,cm^{-2}$, which is higher than in Fig. 9. The Mg densities are about $3\times 10^9\,cm^{-2}$, which is similar to that in Fig. 5. In the equatorial region the Mg columns agree better, and a higher VCD in the nadir results for Mg^+ can be explained by the thermospheric part

of Mg^+ which is not part of the VCD in Fig. 9. At mid latitudes Mg^+ shows a strong seasonal cycle with a summer maximum in Correira et al. (2008). This seasonality is quite symmetric for both hemispheres with higher VCD in the SH. Furthermore, the summer maximum at mid latitudes does not exceed the VCD at low latitudes. For Mg a summer maximum is observed, which is more pronounced in the SH. The Mg^+ to Mg VCD ratios in Correira et al. (2008) are in good agreement with our results shown in Fig. 10.

The nominal limb mode dataset, covering the tangent height range from the surface up to 92 or 105 km (only until early 2003), respectively, combined with the nadir mode dataset from SCIAMACHY from 2002 to 2007 was investigated in Scharringhausen et al. (2008a,b) and Scharringhausen (2007). The peak region for the ions could not be fully resolved with the nominal limb mode, however, qualitatively the agreement between the results by Scharringhausen (2007) (page 69 and 70) and the results from this study for the ions is quite good, showing showing a similar seasonal cycle in the NH, which, however, shows up to a factor 3-4 larger densities and the highest densities at high latitudes, and not at mid latitudes. In the SH the seasonal cycle was not identified well in Scharringhausen (2007), which agreed with the results similar to Fig. 9 when using the pre-flight polarization correction (not shown), which we now found to be wrong (see Sect. 3).

At the very beginning of the Scharringhausen VCD dataset in 2002 (e.g. Figs. 69 and 70 in Scharringhausen, 2007) slightly higher VCD for both species are observed than for the other years. This may come from increased NO signals near the Mg and Mg^+ lines during solar maximum. Another reason for the higher Mg^+ VCD in 2002 may also be related to the change of the maximum tangent altitude from 105 to 92 km.

More differences between our retrievals and the results by Scharringhausen (2007) can be found in the Mg data. This is because the data product retrieved using the Mg line is more affected by the radiative transfer improvements made in this study than the product retrieved using the Mg^+ lines. For example, there was no correction of the Ring effect, the filling in of Fraunhofer lines by inelastic Raman scattering in the Earth's atmosphere (see, e.g. Grainger and Ring (1962)), in Scharringhausen (2007), which led to high densities below 80 km and a density maximum at the lower edge of the retrieval boundaries at 70 km. This inelastic scattering contribution additionally adds a seasonal variation to the dataset.

Furthermore, the Mg line at 285.2 nm is much more affected by self absorption of the emission, which was not considered in Scharringhausen (2007), so the Mg VCD were smaller than reported here. However, most of the important findings from the further analysis of the Scharringhausen data set are only weakly affected by these differences and are still valid.

In summary, it can be concluded that the Mg/Mg^+ results presented here are often in good agreement with previous satellite and rocket instruments. The most striking difference to previous measurements is the strong latitudinal dependence of the peak altitude of Mg^+ with differences of up to 10 km for different latitudes.

7 Comparison of Mg and Mg^+ observed by SCIAMACHY and modelled with WACCM

7.1 WACCM-Mg model

The first global 3D model of magnesium, which is similar to other metals (e.g., Na in Marsh et al. (2013a), Fe in Feng et al. (2013) and K in Plane et al. (2014)), is used to investigate several important questions: for example what injection rate of Mg via the ablation of interplanetary dust particles is needed to explain the absolute Mg and Mg^+ densities; how well can Mg^+ - the only atomic ion to be observed on a global scale - be modelled; and is the coupling of long-range transport and chemistry in the MLT region correctly captured?

WACCM is a high-top chemical-dynamical model, which simulates the altitudes from the Earth's surface up to 140 km (Garcia et al., 2007; Marsh et al., 2007, 2013b). Here we use the specified dynamics SD-WACCM, which is nudged by the GEOS5 meteorological dataset (including temperature, specific humidity, horizontal winds) below 60 km. This is the same version used by Feng et al. (2013), Marsh et al. (2013a) and Plane et al. (2014), who successfully incorporated iron, sodium and potassium chemistry into WACCM.

Here we develop a global model of meteoric magnesium in the atmosphere by combining three components: a treatment of the injection of meteoric constituents into the atmosphere (Feng et al., 2013; Marsh et al., 2013a; Plane et al., 2014), a description of the neutral and ion-molecule chemistry of magnesium in the mesosphere and lower thermosphere (Whalley and Plane, 2010; Plane and Whalley, 2012) and WACCM. The Mg meteoroid injection function (MIF) has a similar seasonal variability as those of Fe and Na. The minimum of the MIF occurs in the spring with an ablation flux of 1300 atoms $cm^{-2} s^{-1}$, and the maximum occurs in the autumn with 2400 $cm^{-2} s^{-1}$ (both at high latitudes). The average flux is $\approx 1850\, cm^{-2} s^{-1}$, which sums up to 32.5 kg d^{-1} over the entire planet. Magnesium constitutes 9.6% of chondritic meteorites by mass, so the equivalent interplanetary dust particle mass is 0.338 t d^{-1}. This is an extremely low number, which indicates that Mg ablates relatively inefficiently from meteoroids.

The peak ablation height is around 95 km. The fluxes are obtained by scaling the Mg MIF to match the observed Mg^+ column density (not to the Mg column density, as Mg^+ is better known from earlier satellite studies). This requires dividing the Mg ablation flux by a factor of 15, relative to that of Na (Marsh et al., 2013a). Since the relative chondritic abundance of Mg is 16 times that of Na, this means that the ablation fluxes of Mg and Na are similar in the model. Similarly, when modelling the Fe layer using WACCM, Feng et al. (2013) had to reduce the Fe MIF relative to Na by a factor of 4. The most likely explanation is that more extreme differential ablation is occurring. As shown in Vondrak et al. (2008) - see Fig. 12 - the more refractory elements such as Mg and Fe ablate less efficiently than Na from slow meteoroids with entry speeds below 20 km s^{-1}.

The MIF used in the present study was calculated from an astronomical dust model where the average speed is around 30 km s^{-1} (see Feng et al. (2013) and Marsh et al. (2013a) for further

details). Hence, one implication of these relatively small injection rates of Mg and Fe is that a significant fraction of meteoroids enter the atmosphere from near-prograde orbits, with speeds close to the minimum of 12 km s^{-1}.

Tables 2–4 list the Mg chemical reactions and their rate coefficients added to the standard chemistry scheme in this study. A schematic diagram of the Mg^+/Mg chemistry appears as Fig. 9 in Plane and Whalley (2012). An important magnesium reservoir on the underside of the Mg layer is $Mg(OH)_2$. This is reduced back to Mg via MgOH by reaction with H atoms (R12a). The subsequent reaction with H atoms (R12b) is most likely faster than R12a, and so the reaction rate is not explicitly listed in table 3 (Plane and Whalley, 2012). The polymerization of MgO_2H_2 to form meteoric smoke is parameterised by a dimerization rate coefficient (reaction R13 in table 3). This reaction should be essentially at the high pressure limit even in the upper mesosphere because of the large number of atoms in the dimer and the large binding energy (268 kJ mol^{-1}, calculated at the B3LYP/6-311+g(2d, p) level of electronic structure theory using the Gaussian 09 program suite (Frisch et al., 2009)). The capture rate coefficient is then increased to $9 \times 10^{-10} cm^3$ $molecule^{-1}$ s^{-1} to account for the concentration of other metallic species (e.g. $NaHCO_3$, FeOH etc.) with which MgO_2H_2 can also polymerize.

The model was run for the period 2004 to 2011, when the GEOS5 analysis data are available. To derive the modeled climatologies of temperature, Mg and other chemical constituents, we use the model output from 2005 to 2011.

7.2 Comparison of WACCM model and SCIAMACHY measurements results

Figure 14 shows the monthly mean results for 7 yr of WACCM simulations of Mg from 2005 to 2011 and Fig. 15 shows the same for Mg^+. Figure 16 shows the VCD for both Mg and Mg^+. Mg shows a clear seasonal cycle with a winter maximum which is most pronounced at the poles. The peak altitude is nearly constant, but small seasonal variations can be found. For example, in February the peak altitude at the poles is roughly 85 km, while it is 5 km higher at 90 km in the equatorial region. Mg^+ shows a seasonal cycle with a summer maximum. In addition, there is an increased Mg^+ density at the poles, even in the winter hemisphere. The Mg^+ peak altitude is close to 95 km and shows no strong variation with latitude and time. The seasonal variations in the VCD profiles for Mg and Mg^+ are very similar to Na and Na^+ profiles (Fig. 3 in Marsh et al., 2013a) and Fe and Fe^+ in Feng et al. (2013).

The geophysical behavior of the Mg and Mg^+ layers can be explained as follows: the abundance of Mg atoms in the layer is governed by the injection flux of Mg atoms, as well as chemical loss and transport through diffusion and advection. The column injection flux of Mg atoms has a seasonal cycle with an autumn maximum most pronounced at the poles where the autumn Mg column injection rate is roughly twice as large as in the spring minimum. The vertical distribution of the metal's injection has a maximum at around 90 km altitude (see, e.g. Vondrak et al. (2008), Fig. 11).

However, the actual height and shape of this injection is not that relevant, as the neutral Mg layer is governed by an ion-molecule cycle on the top-side, and a neutral cycle on the bottom-side, which are fast compared to vertical transport.

The strongest loss processes are the charge transfer reactions of neutral Mg with NO^+ and O_2^+ (R28 and R29 in table 4), which occur mainly at the top of the layer above 90 km, where the concentrations of NO^+ and O_2^+ are large, as well as the reaction with O_3 (R1 in table 3), which has a nearly exponentially increasing density towards lower altitudes, which leads to the largest loss rate at the center and the bottom of the Mg profile. The ozone reaction is fast and several percent of the Mg atoms are converted into MgO within a second. However, this is countered by the reaction of MgO and O to form Mg (R2) and also by reaction R12 on the underside of the layer, which results in a nearly constant amount of Mg atoms in the Mg layer over the diurnal cycle, although the density of the reaction partners, e.g., ozone varies by a factor of 10 between day and night.

There is also the dissociative recombination of Mg-containing ions (R22-R27) on the upper side of the layer, which produces Mg, but is less important for the formation of the Mg layer than the reactions of O and H with neutral reservoir species. More details on the neutral chemistry of Mg, which in summary is complex and does not have only one dominant reservoir species, are discussed by Plane and Whalley (2012). The seasonal cycle is thus a complex coupling of photochemistry involving O, H, O_3 and H_2O and transport (mainly vertical, but horizontal convergence/divergence is also significant at high latitudes). For mid and low latitudes this complex chemistry leads to a low seasonal variation of Mg, which is observed in both SCIAMACHY and WACCM data. Horizontal transport processes are important at high latitudes. At winter high latitudes, which are not observed by SCIAMACHY, WACCM shows a maximum for Mg, which is caused by the convergence of the meridional circulation over the polar vortex. At the summer pole the transport due to the meridional circulation reduces the Mg density.

The seasonal cycle of the Mg^+ layer is more easily explained than that of the Mg layer, and is mainly driven by the availability of the charged main atmospheric constituents NO^+ and O_2^+ for charge exchange reactions. The Mg^+ maximum thus can be found in summer, particular at high latitudes. A summarizing schematic diagram of the neutral and ionized magnesium chemistry is shown in Fig. 9 of Plane and Whalley (2012).

In contrast to the SCIAMACHY measurements, which are made at one particular local time, daily averaged output is used for WACCM in Figs. 14–16. We also co-located the WACCM dataset to SCIAMACHY local time and latitudinal coverage, but found only small differences to the non co-located daily average mean of WACCM (not shown). There is a diurnal variation of the vertical column density in the WACCM data, but nearly no diurnal variation for the the vertical profile shape. Figures 17 and 18 show the direct comparison of SCIAMACHY and WACCM annual means for Mg and Mg^+. We used the co-located data for both plots, since these are the only plots with significant differences between not co-located daily means and co-located data, for latitudes higher than 40°.

Figures 19 and 20 show the comparison for the equatorial vertical profile only.

The peak density of Mg for WACCM in the global annual mean profile is higher than for SCIAMACHY. However, the peak width of the SCIAMACHY profile is larger than for WACCM. Therefore, the VCD of SCIAMACHY and WACCM are similar, which shows, that determining the Mg input rate so that the Mg^+ VCD are in agreement also leads to an agreement in the neutral Mg VCD. The altitude of the maximum number density of Mg at the equator is at 90 km for both SCIAMACHY and WACCM. In the high latitude region, which is only covered by SCIAMACHY in summer, however, the maximum number density altitude of WACCM is about $2-4$ km lower than for SCIAMACHY. Considering the 3.3 km vertical sampling in the SCIAMACHY measurements the $\approx$3.5 km vertical resolution of WACCM in the MLT and the altitude grid step size of 2 km for WACCM and 1 km for SCIAMACHY, this difference is small, but nevertheless significant.

A possible retrieval issue, which might explain the wider SCIAMACHY peak is a strong Ring effect influence (Grainger and Ring, 1962) for the Mg spectral line. At the lower and upper peak edge, the SCIAMACHY number densities are not zero. This may be related to the requirement in the retrievals that the densities must be positive, which is needed for stability in the retrieval. However, the densities are smaller than the single day error there (error estimation for the Mg and Mg^+ dataset has been done by Langowski et al. (2013), e.g. Figs. 21-23). When averaging the data, it must be kept in mind that the error for the close to zero density region does not become smaller, as this is rather a systematic error induced by initial statistical errors, than simply a statistical error.

The agreement of WACCM and SCIAMACHY is better for $\mathrm{Mg^+}$. The WACCM $\mathrm{Mg^+}$ peak and column densities are of similar magnitude as the SCIAMACHY results and also show the same seasonal variability with a summer maximum. There are also small differences: the global density maximum, which is found in the summer hemisphere and which moves over time to the other hemisphere, is not reduced in the WACCM data when passing the equatorial region during equinox and also has a stronger extension to the higher latitudes in summer. In addition, a second maximum appears in the winter hemisphere at high latitudes in the WACCM dataset. SCIAMACHY makes no measurements during polar night and so this second maximum is not observed. The WACCM results do not show the strong seasonality and latitude dependence of the peak altitude, that can be found in the SCIAMACHY results. The peak altitude of 95 km in WACCM is in slightly better agreement with the rocket data than with SCIAMACHY. The differences of the vertical profile of WACCM and SCIAMACHY are small especially at the equator (See, Fig. 20).

The lower peak edge of $\mathrm{Mg^+}$ is in better agreement than for Mg. The impact of the filling-in of the Fraunhofer lines in the atmosphere by rotational Raman scattering by air molecules is much weaker for $\mathrm{Mg^+}$ than for Mg. The agreement of the peak edge becomes worse with larger distance from the peak altitude. Nevertheless, the FWHM of the peak is in good agreement.

A part of the differences between the WACCM results and the SCIAMACHY measurements may be attributed to transport processes of charged particles in electromagnetic fields in the lower ther-

mosphere. The equatorial electron distribution with transport from the equator to higher latitudes has been observed in ionospheric soundings. It is known as the equatorial anomaly or Appleton anomaly (Kendall and Windle, 1965). Typically there are fewer electrons at the equator than at 20° on either side of the equator due to this transport.

Similar transport processes have also been observed for the ions and in situ satellite measurements of the metals above 120 km, e.g. have been carried out using the Atmospheric Explorer satellite. A discussion of this data set can be found in Grebowsky and Aikin (2002).

The vertical upward transport of Mg^+ near the equator has been discussed, e.g. in Hanson and Sterling (1972), which is followed here. The sun is passing the equatorial region from east to west. The ionisation in the thermosphere is strong for low solar zenith angles (SZAs) which leads to denser plasmas there. This leads to a strong electric field from east to west, which results in a strong eastwards current, the so called equatorial electrojet (see, e.g. Forbes (1981)) within $\pm 3°$ around the geomagnetic equator.

The motion of a single charged particle with charge q can be separated into the gyration in the magnetic field $\boldsymbol{B}$, and the motion of the guiding center. For a force $\boldsymbol{F}$, which is perpendicular to the magnetic field, the guiding center moves perpendicular to $\boldsymbol{B}$ and $\boldsymbol{F}$ with the drift velocity $\boldsymbol{v} = \frac{1}{q}\frac{\boldsymbol{F}\times\boldsymbol{B}}{B^2}$. Using the Lorentz force $\boldsymbol{F} = q\boldsymbol{E}$ results in the drift velocity $\boldsymbol{v} = \frac{\boldsymbol{E}\times\boldsymbol{B}}{B^2}$. This drift is called $\boldsymbol{E}\times\boldsymbol{B}$-Drift (see, e.g. the textbook of Chen (1984)).

The magnetic field along the meridians and the electric field along the equator lead to an $\boldsymbol{E}\times\boldsymbol{B}$-Drift perpendicular to both fields into the radial direction, which lifts both electrons and ions into higher altitude regions and even above the F-layer. However, because of the limited extent of the equatorial electrojet, this effect can only explain an upward transport of Mg^+ within $\pm 3°$ N geomagnetic latitude. Fesen et al. (1983) showed that additionally neutral meridional winds have to be taken into account in order to explain vertical transport also at higher latitudes up to 30° and this was experimentally shown, e.g. in Fesen and Hays (1982a,b) and Gérard and Monfils (1978).

The annual means of SCIAMACHY Mg^+densities (see Fig. 7) show higher densities above 110 km at the northernmost and southernmost latitudes due to less coverage and therefore higher statistical errors. However, at high northern latitudes and at the ascending node side, which is cut off in the shown results, high densities are retrieved when also using the stray-light contaminated measurements. This is shown in Fig. 21. The results as well as the input raw data show low densities below 90 km and at different altitudes in between the high signal region, which makes a differentiation between a stray-light effect and a true metal emission complicated. Should this feature be real it could be explained by the cleft ion fountain found by Lockwood et al. (1985), which describes the transport of charged particles along the magnetic field lines, which strongly converge at the pole. This transport may lift charged particles up to several Earth radii until they become neutralized and sink down if they are heavy enough and are not quickly ionized again.

8 Mg, Mg^+ and noctilucent clouds

Metal chemistry plays a role in the generation of nucleation nuclei required for the formation of NLC. Consequently it is interesting to investigate the change of the Mg and Mg^+ layers in the vicinity of NLC. The vertical profile shape of Mg at around 70° N shown in Fig. 22 changes during the summer and shows a weak uplift and thinning of the layer (especially in June and July), which however is hard to qualify as significant, as Mg shows strong variations and in addition the latitudinal edge region of the retrieval bears potential for systematic errors, since, e.g. the latitudinal smoothing constraint used does not work well at the edge. An uplift of the layer, may also be attributed to transport due to the upper mesospheric meridional circulation (Note that in Figs. 22 and 24 less data is cut out at the high latitudes, so that more months are covered, with the tradeoff of more edge artifacts, especially in the south).

The VCD, however, is significantly reduced at polar latitudes during the summer and the reduction is stronger in the NH than in the SH. In contrast to the WACCM-Mg model results Mg^+ does not show the highest densities in summer at high latitudes, but at mid latitudes. NLC, which are not considered in WACCM-Mg, occur at polar latitudes during a 3 month period in the summer hemisphere.

NLC can be detected in many different ways. For example they show an increased amplitude of backscattered radiation at the altitude of their appearance. This is used here to quantisize the amount of NLC. A two step algorithm is used (for details see Langowski (2014)). First it is determined whether a NLC is detected at all. Afterwards the amount of NLC is determined only for the cases, where a NLC is identified, as otherwise this quantification produces wrong results. The quantification is illustrated in Fig. 23. At a certain wavelength window (here we use 458 to 552 nm), where the signal is dominated mainly by Rayleigh-scattering the average signal is formed for each tangent altitude of the MLT-measurements. NLC are typically observed as peaks at around 84 km. The background spectra, which results only from Rayleigh-scattering without NLC is fitted and subtracted from the limb radiance. The remaining signal is summed up and the resulting quantity is called NLC radiance here.

VCD of Mg and Mg^+ and the NLC radiance are shown in Fig. 24. The NLC radiance is well anticorrelated with both the Mg and Mg^+ densities at high latitudes. However, this does not unambiguously imply that the lower VCD of Mg and Mg^+ are dominated by Mg being taken up by NLC particles, as other effects may play a more dominant role. For example, the seasonal variation with a summer minimum for Mg is even more pronounced in the WACCM-Mg (also for Na and Fe) model, which does not consider NLC, than in the SCIAMACHY results and in the SCIAMACHY results the Mg density is also reduced at regions, e.g. $50°$N in April, where no NLC occur. The Mg^+ layer is formed at the top of the NLC particle region and only weakly overlaps with the region, where NLC are formed. Furthermore Lorentz force induced upward transport may reduce the Mg^+ density at the poles.

In summary it is interesting to note that the VCD of both Mg and Mg^+ are lower in summer during NLC episodes but further investigations are needed to understand the origin of the lower Mg and Mg^+ densities to decide whether loss to NLC or other processes are dominant.

9 Summary and conclusions

Monthly averaged global vertical and latitudinal density distributions of Mg and Mg^+ retrieved from the SCIAMACHY limb MLT-measurements from 2008 to 2012 have been shown. The MLT-measurements cover the vertical region between 70 km and 150 km and have a good vertical resolution in the peak region.

Mg shows highly variable results and variability is mostly affected by the measurement error and no clear seasonal cycle can be observed for Mg, apart from the northern high latitudes where a summer minimum is observed. The peak altitude of Mg is nearly constant at around 90 km for all latitudes and times.

Mg^+ shows a clear seasonal cycle with a summer maximum in the peak density, most pronounced at mid latitudes. Mg^+ shows a seasonal variation of the peak altitude with higher altitudes in the summer, as well as a latitudinal dependence of the peak altitudes with up to 5–10 km higher altitudes at mid latitudes compared to the equatorial peak altitude of 95 km.

The SCIAMACHY results are reasonably consistent with previously published rocket profiles and significantly extend the amount of data of Mg and Mg^+. The peak density values and the observed seasonality for Mg^+ are in good agreement. However, the rocket measurements do not show the latitudinal dependence of the peak altitude, but typically show peak altitudes at slightly below 95 km.

The SCIAMACHY results were compared with WACCM-Mg model results. For Mg WACCM shows a clearer seasonal cycle with a winter maximum at the poles than SCIAMACHY. The WACCM Mg peak densities are roughly a factor 2-3 bigger than the SCIAMACHY peak densities. The peak altitude and peak shape are in good agreement with SCIAMACHY, which shows a slightly wider profile. The combination of higher peak densities for WACCM, but wider peak profile for SCIAMACHY leads to very similar values for the VCD.

The agreement between WACCM and SCIAMACHY is generally better for Mg^+ than for Mg. Both SCIAMACHY and WACCM Mg^+ results show a clear seasonal cycle with a summer maximum and the peak densities are in good agreement. However, similar to the limited number of the rocket measurements, WACCM does not show a latitudinal dependence of the peak altitude. The peak shape of Mg^+ agrees well for WACCM and SCIAMACHY in the high density region, where the SCIAMACHY error is low.

During the arctic summer Mg and Mg^+ show a density minimum at high latitudes. This is in coincidence with the occurence of NLC, but our results do not allow the conclusion that the Mg and Mg^+ reduction at high latitudes during summer is related to the occurrence of NLC. Further

investigations involving model simulations are required to address this question.

Acknowledgements. We wish to thank AFOSR and EOARD for the financial support of the project (grant#FA8655-09-3012). SCIAMACHY is jointly funded by Germany, the Netherlands and Belgium. This work was in part supported by the University of Bremen and Ernst-Moritz-Arndt-University of Greifswald and by the ESA MesosphEO project. SCIAMACHY data was kindly provided by the European Space Agency (ESA). The WACCM-Mg modelling work was supported by the UK Natural Environment Research Council (NERC grant NE/G019487/1) and the European Research Council (project number 291332-CODITA). The National Center for Atmospheric Research is operated by the University Corporation for Atmospheric Research under sponsorship of the National Science Foundation.

References

Aikin, A. C. and Goldberg, R. A.: Metallic ions in the equatorial ionosphere, J. Geophys. Res., 78, 734–745, 1973.

Anderson, J. G. and Barth, C. A.: Rocket investigation of the Mg I and Mg II dayglow, J. Geophys. Res., 76, 3723–3732, 1971.

Bender, S., Sinnhuber, M., Burrows, J. P., Langowski, M., Funke, B., and López-Puertas, M.: Retrieval of nitric oxide in the mesosphere and lower thermosphere from SCIAMACHY limb spectra, Atmos. Meas. Tech., 6, 2521–2531, doi:10.5194/amt-6-2521-2013, 2013.

Boksenberg, A. and Gérard, J. C.: Ultraviolet observations of equatorial dayglow above the F_2 Peak, J. Geophys. Rev., 78, 4641–4650, 1973.

Bovensmann, H., Burrows, J. P., Buchwitz, M., Frerick, J., Noël, S., Rozanov, V. V., Chance, K. V., and Goede, A. P. H.: SCIAMACHY: mission objectives and measurement modes, J. Atmos. Sci., 56, 127–150, 1999.

Brown, P. and Jones, J.: A determination of the strengths of the sporadic radio-meteor sources, Earth Moon Planets, 68, 223–245, 1995.

Burrows, J. P., Hölzle, E., Goede, A. P. H., Visser, H., and Fricke, W.: SCIAMACHY–scanning imaging absorption spectrometer for atmospheric chartography, Acta Astronaut., 35, 445–451, 1995.

Ceplecha, Z., Borovička, J., Elford, W. G., Revelle, D. O., Hawkes, R. L., Porubčan, V., and Šimek, M.: Meteor phenomena and bodies, Space Sci. Rev., 84, 327–471, 1998.

Chandrasekhar, S.: Radiative Transfer, Dover Publ., New York, 1960.

Chen, F. F.: Introduction to plasma physics and controlled fusion volume 1: plasma physics, 2nd ed., Springer, New York, 1984.

Correira, J.: Temporal and Spatial Distribution of Metallic Species in the Upper Atmosphere, Ph.D. thesis, The Catholic Unversity of America, Washington D.C., 134 pp., 2009.

Correira, J., Aikin, A. C., Grebowsky, J. M., Pesnell, W. D., and Burrows, J. P.: Seasonal variations of magnesium atoms in the mesosphere-thermosphere, Geophys. Res. Lett., 35, 330–337, 2008.

Correira, J., Aikin, A. C., Grebowsky, J. M., and Burrows, J. P.: Metal concentrations in the upper atmosphere during meteor showers, Atmos. Chem. Phys., 10, 909–917, doi:10.5194/acp-10-909-2010, 2010.

Curtius, J., Weigel, R., Vössing, H.-J., Wernli, H., Werner, A., Volk, C.-M., Konopka, P., Krebsbach, M., Schiller, C., Roiger, A., Schlager, H., Dreiling, V., and Borrmann, S.: Observations of meteoric material and implications for aerosol nucleation in the winter arctic lower stratosphere derived from in situ particle measurements, Atmos. Chem. Phys., 5, 3053–3069, doi:10.5194/acp-5-3053-2005, 2005.

Feng, W., Marsh, D. R., Chipperfield, M. P., Janches, D., Hoffner, J., Yi, F., and Plane, J. M. C.: A global atmospheric model of meteoric iron, J. Geophys. Res.-Atmos., 118, 9456–9474, 2013.

Fentzke, J. T. and Janches, D.: A semi-empirical model of the contribution from sporadic meteoroid sources on the meteor input function observed at arecibo, J. Geophys. Res., 113, A03304, doi:10.1029/2007JA012531, 2008.

Fesen, C. G., and Hays, P. B.: Mg^+ Morphology from visual airglow experiment observations, J. Geophys. Res., 87, 9217–9223, 1982a.

Fesen, C. G., and Hays, P. B.: Two-dimensional inversion technique for satellite airglow data, Appl. Optics, 21,

3784–3791, 1982b.

Fesen, C. G., Hays, P. B., and Anderson, D. N.: Theoretical Modelling of Low-Latitude Mg^+, J. Geophys. Res., 88, 3211–3223, 1983.

Flynn, G.: Chapter 4 in: Meteors in the Earth's Atmosphere, edited by: Murad, E. and Williams, I. P., Cambridge University Press, Cambridge, 2002.

Forbes, J. M.: The equatorial electrojet, Rev. of Geophys., 19, 469–504, 1981.

Frisch, M., Trucks, G., Schlegel, H., Scuseria, G., Robb, M., Cheeseman, J., Scalmani, G., Barone, V., Mennucci, B., Petersson, G., Nakatsuji, H., Caricato, M., Li, X., Hratchian, H., Izmaylov, A., Bloino, J., Zheng, G., Sonnenberg, J., Hada, M., Ehara, M., Toyota, K., Fukuda, R., Hasegawa, J., Ishida, M., Nakajima, T., Honda, Y., Kitao, O., Nakai, H., Vreven, T., J. A. Montgomery, J., Peralta, J., Ogliaro, F., Bearpark, M., Heyd, J., Brothers, E., Kudin, K., Staroverov, V., Kobayashi, R., Normand, J., Raghavachari, K., Rendell, A., Burant, J., Iyengar, S., Tomasi, J., Cossi, M., Rega, N., Millam, J., Klene, M., Knox, J., Cross, J., Bakken, V., Adamo, C., Jaramillo, J., Gomperts, R., Stratmann, R., Yazyev, O., Austin, A., Cammi, R., Pomelli, C., Ochterski, J., Martin, R., Morokuma, K., Zakrzewski, V., Voth, G., Salvador, P., Dannenberg, J., Dapprich, S., Daniels, A., Farkas, O., Foresman, J., Ortiz, J., Cioslowski, J., and Fox, D.: Gaussian 09, Revision A.1, Gaussian Inc., available at: www.gaussian.com (14 November 2011), 2009.

Garcia, R. R., Marsh, D. R., Kinnison, D. E., Boville, B. A., and Sassi, F.: Simulation of secular trends in the middle atmosphere, 1950–2003, J. Geophys. Res., 112, D09301, doi:10.1029/2006JD007485, 2007.

Gardner, J. A., Viereck, R. A., Murad, E., Knecht, J., Pike, C. P., Broadfoot, A. L., and Anderson, E. R.: Simultaneous observations of neutral and ionic magnesium in the thermosphere, Geophys. Res. Lett., 22, 2119–2122, 1995.

Gardner, J. A., Broadfoot, A. L., McNeil, W. J., Lai, S. T., and Murad, E.: Analysis and modeling of the GLO-1 observations of meteoric metals in the thermosphere, J. Atmos Sol.-Terr. Phy., 61, 542–562, 1999.

Gardner, C. S., Liu, A. Z., Marsh, D. R., Feng, W., and Plane, J. M. C.: Inferring the Global Cosmic Dust Influx to the Earth's Atmosphere from Lidar Observations of the Vertical Flux of Mesospheric Na , J. Geophys. Res. – Space Physics, doi:10.1002/2014JA020383, 2014.

Gérard, J. C. and Monfils, A.: Satellite Observations of the Equatorial Mg II Dayglow Intensity Distribution, J. Geophys. Rev., 79, 2544–2550, 1974.

Gérard, J. C. and Monfils, A.: The MgII Equatorial Airglow Altitude Distribution, J. Geophys. Res., 83, 4389–4391, 1978.

Grainger, J. and Ring, J.: Anomalous Fraunhofer Line Profiles, Nature, 193, 762, 1962.

Grebowsky, J. M. and Aikin, A. C.: Chapter 8 in: Meteors in the Earth's Atmosphere, edited by: Murad, E. and Williams, I. P., Cambridge University Press, Cambridge, 2002.

Grebowsky, J. M., Goldberg, R. A., and Pesnell, W. D.: Do meteor showers significantly perturb the ionosphere?, J. Atmos. Sol.-Terr. Phy., 60, 607–615, 1998.

Hamilton, D. R.: The resonance radiation induced by elliptically polarized light, Astrophys. J., 106, 457–465, 1947.

Hanson, W. B. and Sterling, D. L.: Source and Identification of Heavy Ions in the Equatorial F Layer, J. Geophys. Res., 77, 5530–5541, 1972.

Herrmann, U., Eberhardt, P., Hidalgo, M. A., and Kopp, E.: Metal ions and isotopes in sporadic E-layer during

Perseid meteor shower, Space Res., 18, 249–252, 1978.

Hunten, D. M., Turco, R. P., and Toon, O. B.: Smoke and dust particles of meteoric origin in the mesosphere and stratosphere, J. Atmos. Sci., 37, 1342–1357, 1980.

Istomin, V.: Ions of extra-terrestrial origin in the earth's ionosphere, Planet. Space Sci., 11, 173–181, 1963.

Janches, D., Heinselman, C., Chau, J., Chandran, A., and Woodman, R.: Modeling the global micrometeor input function in the upper atmosphere observed by high power and large aperture radars, J. Geophys. Res., 111, A07317, doi:10.1029/2006JA011628, 2006.

Janches, D., Dyrud, L. P., Broadley, S. L., and Plane, J. M. C.: First observations of micrometeoroid differential ablation in the atmosphere, Geophys. Res. Lett., 36, L06101, doi:10.1029/2009GL037389, 2009.

Jenniskens, P.: Meteor Showers and Their Parent Comets, Cambridge University Press, Cambridge, 2006.

Johnson, C. Y. and Meadows, E. B.: First Investigation of Ambient Positive-Ion Composition to 219 km by Rocket-Borne Spectrometer, J. Geophys. Res., 60, 193–203, 1955.

Joiner, J. and Aikin, A. C.: Temporal and spatial variations in upper atmospheric Mg^+, J. Geophys. Res., 101, 5239–5250, 1996.

Kalashnikova, O., Horanyi, M., Thomas, G. E., and Toon, O. B.: Meteoric smoke production in the atmosphere, Geophys. Res. Lett., 27, 3293–3296, 2000.

Kendall, P. C. and Windle, D. W.: The Appleton anomaly, Nature, 207, 964–965, 1965.

Kopp, E.: On the abundance of metal ions in the lower ionosphere, J. Geophys. Res., 102, 9667–9674, 1997.

Kopp, E. and Herrmann, U.: Ion composition in the lower ionosphere, Ann. Geophys., 2, 83–94, 1984.

Kopp, E., Eberhardt, U., Herrmann, U., and Björn, L.: Positive ion composition of the high latitude summer D-region with noctilucent clouds, J. Geophys. Res., 90, 13041–13053, 1985a.

Kopp, E., Ramseyer, H., and Björn, L.: Positive ion composition and electron density in a combined auroral and NLC event, Adv. Space. Res., 4, 157–161, 1985b.

Kramida, A., Ralchenko, Y., Reader, J., and NIST ASD Team: NIST Atomic Spectra Database (version 5.0), National Institute of Standards and Technology, Gaithersburg, MD, 2012.

Krijger, J. M., Snell, R.,van Harten, G., Rietjens, J. H. H., and Aben, I.: Mirror contamination in space I: approach, Atmos. Meas. Tech. Discuss., 7, 1213-1246, 2014.

Langowski, M., Sinnhuber, M., Aikin, A. C., von Savigny, C., and Burrows, J. P.: Retrieval algorithm for densities of mesospheric and lower thermospheric metal atom and ion species from satellite borne limb emission signals, Atmos. Meas. Tech., 7, 29–48, doi:10.5194/amt-7-29-2014, 2014.

Langowski, M.: Investigation of metal atoms and ions in the mesosphere and lower thermosphere by satellite remote sensing with SCIAMACHY/Envisat, Ph. D. thesis, 2014.

Liebing, P., Bramstedt, K., Noël, S, Rozanov, V., Bovensmann,¸ H., and Burrows, J. P.: Polarization data from SCIAMACHY limb backscatter observations compared to vector radiative transfer model simulations, Atmos. Meas. Tech., 6, 1503-1520, 2013.

Lockwood, M., Horwitz, J. R., Chandler, M. O., Waite, J. H., Moore, T. E., and Chappel, C. R.: The cleft ion fountain, J. Geophys. Res., 90, 9736–9748, 1985.

Marsh, D. R., Garcia, R. R., Kinnison, D. E., Boville, B. A., Sassi, F., Solomon, S. C., and Matthes, K.: Modeling the whole atmosphere response to solar cycle changes in radiative and geomagnetic forcing, J. Geophys. Res., 112, D23306, doi:10.1029/2006JD008306, 2007.

Marsh, D. R., Janches, D., Feng, W., and Plane, J. M. C.: A global model of meteoric sodium, J. Geophys. Res.-Atmos., 118, 11442–11452, doi:10.1002/jgrd.50870, 2013a.

Marsh, D. R., Mills, M. J., Kinnison., D. E., Lamarque, J. F., Calvo, N., and Polvani, L. M.: Climate Change from 1850 to 2005 Simulated in CESM1(WACCM), J. Climate, 26, 7372–7391, doi:10.1175/JCLI-D-12-00558, 2013b.

Martínez-Núñez, E., Whalley, C. L., Shalashilin, D., and Plane, J. M. C.: Dynamics of Mg^++H_2O+He: Capture, collisional stabilization and collision-induced dissociation, J. Phys. Chem. A, 114, 6472–6479, doi:10.1021/jp102454j, 2010.

Mathews, J. D., Janches, D., Meisel, D. D., and Zhou, Q.-H.: The micrometeoroid mass flux into the upper atmosphere: Arecibo results and a comparison with prior estimates, Geophys. Res. Lett., 28, 1929–1932, 2001.

McNeil, W. J., Lai, S. T., and Murad, E.: Differential ablation of cosmic dust and implications for the relative abundances of atmospheric metals, J. Geophys. Res., 103, 10899–10911, 1998.

Mende, S. B., Swenson, G. R., and Miller, K. L.: Observations of E and F Region Mg^+ from Spacelab 1, J. Geophy. Res., 90, 6667–6673, 1985.

Minschwaner, K., Herceg, D., Budzien, S. A., Dymond, K. F., Fortna, C., and P., M. R.: Observations of middle ultraviolet emissions in the middle and lower thermosphere: NO, O_2, O and Mg^+, J. Geophys. Res., 112, A10311, 2007.

Murad, E. and Williams, I. P.: Meteors in the Earth's atmosphere, Cambridge University Press, Cambridge, 2002.

Narcisi, R. S.: Composition studies of the lower ionosphere, in: Physics of the Upper Atmosphere, edited by: Verniani, F., Editrice Compositori, Bologna, p. 12, 1971.

Narcisi, R. S. and Bailey, A. D.: Mass spectrometric measurements of positive ions at altitudes from 64 to 112 kilometers, J. Geophys. Res., 70, 3687–3700, 1965.

Nesvorný, D., Jenniskens, P., Levison, H. F., Bottke, W., Vokrouhlický, D., and Gounelle, M.: Cometary origin of the Zodiacal Cloud and carbonaceous micrometeorites, implications for hot debris disks, Astrophys. J., 713, 816–836, 2010.

Nesvorný, D., Janches, D., Vokrouhlický, P., Pokorný, P., Bottke, W. F., and Jenniskens, P.: Dynamical model for the zodiacal cloud and sporadic meteors, Astrophys. J., 743, 129, 2011a.

Nesvorný, D., Vokrouhlický, P., Pokorný, P., and Janches, D.: Dynamics of dust particles released from oort cloud comets and their contribution to radar meteors, Astrophys. J., 743, 37, 2011b.

Philbrick, C. R., Narcisi, R. S., Good, R., Hoffmann, H. S., Keneshea, T. J.,MacLeod, M., A., Zimmermann, S. P., and Reinisch, B. W.: The Aladdin Experiment – Part II, Composition, Space Res., VII, 441–449, 1973.

Plane, J. M. C.: Atmospheric chemistry of meteroric metals, Chem. Rev., 103, 4963–4984, 2003.

Plane, J. M. C.: Cosmic dust in the earth's atmosphere, J. Atmos. Sol.-Terr. Phy., 41, 6507–6518, 2012.

Plane, J. M. C., Feng, W., Dawkins. E., Chipperfield, M. P. C., Höffner, J., Janches, D. and Marsh, D. R.: Resolving the strange behaviour of extra-terrestrial potassium in the upper atmosphere, Geophys. Res. Lett., doi:10.1002/2014GL060334, 2014.

Plane, J. M. C. and Helmer, M.: Laboratory Study of Reactions $Mg + O_3$ and $MgO + O_3$, implications for the

chemistry of magnesium in the upper atmosphere, Faraday Discuss., 100, 411–430, 1995.

Plane, J. M. C. and Whalley, C. L.: A new model for magnesium chemistry in the upper atmosphere, J. Phys. Chem. A, 116, 6240–6252, 2012.

Rapp, M and Thomas, G. E.: Modelling the microphysics of mesospheric ice particles: Assessment of current capabilities and basic sensitivities, J. Atm. Sol. Terr. Phys., 68, 715-744, 2006.

Roddy, P. A., Earle, G. D., Swenson, C., Carlson, C. G., and Bullett, T. W.: Relative concentrations of molecular and metallic ions in the midlatitude intermediate and sporadic-E layers, Geophys. Res. Let., 31, L19807, 2004.

Rollason, R. J. and Plane, J. M. C.: A kinetic study of the reactions of MgO with H_2O, CO_2 and O_2: implications for magnesium chemistry in the mesosphere, Phys. Chem. Chem. Phys., 3, 4733–4740, 2001.

Rozanov, V. V., Rozanov, A. V., Kokhanovsky, A. A., and Burrows, J. P.: Radiative transfer through terrestrial atmosphere and ocean: Software package SCIATRAN, J. Quant. Spect. Rad. Trans. 133, 13–71, doi:10.5194/acp-8-1963-2008, 2014.

Rutherford, J. A., Mathis, R. F., Turner, B. R. and Vroom, D. A.: Formation of Magnesium ions by charge transfer, J. Chem. Phys., 55, 3785–3793, 1971.

Saunders, R. W. and Plane, J. M. C.: A laboratory study of meteor smoke analogues: composition, optical properties and growth kinetics, J. Atmos. Sol.-Terr. Phy., 68, 550–553, 2006.

Scharringhausen, M.: Investigation of Mesospheric and Thermospheric Magnesium Species from Space, Ph.D. thesis, Universität Bremen, Bremen, Germany, 2007.

Scharringhausen, M., Aikin, A. C., Burrows, J. P., and Sinnhuber, M.: Space-borne measurements of mesospheric magnesium species – a retrieval algorithm and preliminary profiles, Atmos. Chem. Phys., 8, 1963–1983, doi:10.5194/acp-8-1963-2008, 2008a.

Scharringhausen, M., Aikin, A. C., Burrows, J. P., and Sinnhuber, M.: Global column density retrieval of mesospheric and thermospheric MgI and MgII from SCIAMACHY limb and nadir radiance data, J. Geophys. Res., 113, D13303, doi:10.1029/2007JD009043, 2008b.

Swider, W.: Ionic and neutral concentrations of Mg and Fe near 92 km, Planet. Space Sci., 32, 307–312, 1984.

Voigt, C., Schlager, H, Luo, B. P., Dörnbrack, A., Roiger, A., Stock, P., Curtius, J.,Vössing, H., Borrmann, S., Davies, S., Konopka, P., Schiller, C., Shur, G., and Peter, T.: Nitric Acid Trihydrate (NAT) formation at low NAT supersaturation in Polar Stratospheric Clouds (PSC), Atmos. Chem. Phys., 5, 1371–1381, doi:10.5194/acp-5-1371-2005, 2005.

von Savigny, C., Kaiser, J. W., Bovensmann, H., Burrows, J. P., McDermid, I. S., and Leblanc, T.: Spatial and temporal characterization of SCIAMACHY limb pointing errors during the first three years of the mission, Atmos. Chem. Phys., 5, 2593–2602, doi:10.5194/acp-5-2593-2005, 2005.

von Savigny, C., Bovensmann, H., Bramstedt, K., Dikty, S., Ebojie, F., Jones, A., Noël, S., Rozanov, A., and Sinnhuber, B.-M.: Indications for long-term trends and seasonal variations in the SCIAMACHY Level 1 version 6.03 tangent height information, Techn. Note-IUP-scia-pointing-2009-01, University of Bremen, Bremen, Germany, Issue 2, 2009.

Vondrak, T., Plane, J. M. C., Broadley, S., and Janches, D.: A chemical model of meteoric ablation, Atmos. Chem. Phys., 8, 7015–7031, doi:10.5194/acp-8-7015-2008, 2008.

Whalley, C. L. and Plane, J. M. C.: Meteoric ion layers in the Martian atmosphere, Faraday Discuss., 147,

Table 1. Original sources and geolocations of plots in Fig. 11.

No.	Lat	Lon	Date	Original reference	Taken from
1	mid N	U.S.S.R.(Eur)	June 15 1960	Istomin (1963)	Istomin (1963)
2	30 N	86 W	October 31 1963	Narcisi and Bailey (1965)	Narcisi and Bailey (1965)
3	30 N	86 W	April 12 1967	Narcisi (1971)	Grebowsky and Aikin (2002)
4	30 N	86 W	April 12 1967	Narcisi (1971)	Grebowsky and Aikin (2002)
5	8 N	77 E	March 19 1970	Aikin and Goldberg (1973)	Aikin and Goldberg (1973)
6	8 N	77 E	March 19 1970	Aikin and Goldberg (1973)	Aikin and Goldberg (1973)
7	8 N	77 E	March 9 1970	Aikin and Goldberg (1973)	Aikin and Goldberg (1973)
8	8 N	77 E	March 10 1970	Aikin and Goldberg (1973)	Aikin and Goldberg (1973)
9	30 N	86 W	November 20 1970	Philbrick et al. (1973)	Grebowsky and Aikin (2002)
10	40 N	9 E	December 14 1971	Zbinden et al. (1975)	Zbinden et al. (1975)
11	38 N	75 W	August 12 1976	Herrmann et al. (1978)	Kopp (1997)
12	51 N	93 W	February 24 1979	Kopp and Herrmann (1984)	Kopp (1997)
13	67 N	20 E	November 30 1980	Kopp et al. (1985b)	Kopp (1997)
14	67 N	20 E	August 13 1978	Kopp et al. (1985a)	Kopp (1997)
15	38 N	75 W	July 1 2003	Roddy et al. (2004)	Roddy et al. (2004)
16	$\pm$ 20 N	all	Oct 15 - Nov 29 1999	Minschwaner et al. (2007)	Minschwaner et al. (2007)

Table 2. Magnesium Photolysis Chemistry added into WACCM.

No.	Reaction	Rate/s^{-1}	Reference
J1	$Mg + h\nu \rightarrow Mg^+ + e^-$	$j_1 = 4 \times 10^{-7}$	Swider (1984)

349–368, 2010.

Whalley, C. L., Gómez Martín, J. C., Wright, T. G. and Plane, J. M. C.: A kinetic study of Mg^+ and Mg-containing ions reacting with O_3, O_2, N_2, CO_2, N_2O and H_2O, implications for magnesium ion chemistry in the upper atmosphere, Phys. Chem. Chem. Phys., 13, 6352–6364, doi:10.1039/c0cp02637a, 2011.

Zbinden, P. A., Hidalgo, M. A., Eberhardt, P., and Geiss, J.: Mass spectrometer measurements of the positive ion composition in the D- and E-Regions of the ionosphere, Planet. Space Sci., 23, 1621–1642, 1975.

Table 3. Neutral chemistry of magnesium added into WACCM.

No.	Reaction	Rate/$\mathrm{cm^3\,molecule^{-1}\,s^{-1}}$	Reference
R1	$\mathrm{Mg + O_3 \rightarrow MgO + O_2}$	$k_1 = 2.3\times10^{-10}\exp(-139/T)$	Plane and Helmer (1995)
R2	$\mathrm{MgO + O \rightarrow Mg + O_2}$	$k_2 = 6.2\times10^{-10}\times(T/295)^{0.167}$	Whalley and Plane (2010)
R3	$\mathrm{MgO + O_3 \rightarrow MgO_2 + O_2}$	$k_3 = 2.2\times10^{-10}\exp(-548/T)$	Plane and Helmer (1995)
R4	$\mathrm{MgO_2 + O \rightarrow MgO + O_2}$	$k_4 = 7.9\times10^{-11}\exp(T/295)^{0.167}$	Whalley and Plane (2010)
R5	$\mathrm{MgO + H_2O + \mathit{M} \rightarrow MgO_2H_2 + M}$	$k_5 = 1.1\times10^{-26}\times(T/200)^{-1.59}$	Rollason and Plane (2001)
R6	$\mathrm{MgO_3 + H_2O \rightarrow MgO_2H_2 + O_2}$	$k_6 = 1.0\times10^{-12}$	Rollason and Plane (2001)
R7	$\mathrm{MgO + O_2 + M \rightarrow MgO_3 + M}$	$k_7 = 3.8\times10^{-29}\times(T/200)^{-1.59}$	Rollason and Plane (2001)
R8	$\mathrm{MgO + CO_2 + M \rightarrow MgCO_3 + M}$	$k_8 = 5.9\times10^{-29}\times(T/200)^{-0.86}$	Rollason and Plane (2001)
R9	$\mathrm{MgCO_3 + O \rightarrow MgO_2 + CO_2}$	$k_9 = 6.7\times10^{-12}$	Plane and Whalley (2012)
R10	$\mathrm{MgO_2 + O_2 + M \rightarrow MgO_4 + M}$	$k_{10} = 1.8\times10^{-26}\times(T/200)^{-2.5}$	Plane and Whalley (2012)
R11	$\mathrm{MgO_4 + O \rightarrow MgO_3 + O_2}$	$k_{11} = 8.0\times10^{-14}$	Plane and Whalley (2012)
R12a	$\mathrm{MgO_2H_2 + H \rightarrow MgOH + H_2O}$	$k_{12} = 1.0\times10^{-11}\times\exp(-600/T)$	Plane and Whalley (2012)
R12b	$\mathrm{MgOH + H \rightarrow Mg + H_2O}$	faster than R12a	see text
R13	$\mathrm{MgOH + MgOH \rightarrow Mg_2O_2H_2}$	$k_{13} = 9.0\times10^{-10}$	see text
R14	$\mathrm{MgO_3 + H \rightarrow MgOH + O_2}$	$k_{14} = 2.0\times10^{-12}$	Plane and Whalley (2012)
R15	$\mathrm{MgO_3 + O \rightarrow MgO_2 + O_2}$	$k_{15} = 1.0\times10^{-13}$	Plane and Whalley (2012)

Table 4. Ion-molecule chemistry of magnesium added into WACCM.

No.	Reaction	Rate/$\mathrm{cm^3\,molecule^{-1}\,s^{-1}}$	Reference
R16	$\mathrm{Mg^+ + O_3 \rightarrow MgO^+ + O_2}$	$k_{16} = 1.2\times10^{-9}$	Whalley et al. (2011)
R17	$\mathrm{MgO^+ + O \rightarrow Mg^+ + O_2}$	$k_{17} = 5.9\times10^{-10}$	Whalley and Plane (2010)
R18	$\mathrm{MgO^+ + O_3 \rightarrow Mg^+ + 2O_2}$	$k_{18} = 1.8\times10^{-10}$	Whalley et al. (2011)
R19	$\mathrm{MgO^+ + O_3 \rightarrow MgO_2^+ + O_2}$	$k_{19} = 3.3\times10^{-10}$	Whalley et al. (2011)
R20	$\mathrm{Mg^+ + N_2 + M \rightarrow MgN_2^+ + M}$	$k_{20} = 1.8\times10^{-30}(T/200)^{-1.72}$	Whalley et al. (2011)
R21	$\mathrm{Mg^+ + O_2 + M \rightarrow MgN_2^+ + M}$	$k_{21} = 2.4\times10^{-30}(T/200)^{-1.65}$	Whalley et al. (2011)
R22	$\mathrm{MgN_2^+ + e^- \rightarrow Mg + N_2}$	$k_{22} = 3.0\times10^{-7}(T/200)^{-0.5}$	Plane and Whalley (2012)
R23	$\mathrm{MgCO_2^+ + e^- \rightarrow Mg + CO_2}$	$k_{23} = 3.0\times10^{-7}(T/200)^{-0.5}$	Plane and Whalley (2012)
R24	$\mathrm{MgH_2O^+ + e^- \rightarrow Mg + H_2O}$	$k_{24} = 3.0\times10^{-7}(T/200)^{-0.5}$	Plane and Whalley (2012)
R25	$\mathrm{MgO^+ + e^- \rightarrow Mg + O}$	$k_{25} = 3.0\times10^{-7}(T/200)^{-0.5}$	Plane and Whalley (2012)
R26	$\mathrm{MgO_2^+ + e^- \rightarrow Mg + O_2}$	$k_{26} = 3.0\times10^{-7}(T/200)^{-0.5}$	Plane and Whalley (2012)
R27	$\mathrm{Mg^+ + e^- \rightarrow Mg + \mathit{h\nu}}$	$k_{27} = 1.0\times10^{-12}$	Plane and Helmer (1995)
R28	$\mathrm{Mg + O_2{}^+ \rightarrow Mg^+ + O_2}$	$k_{28} = 1.2\times10^{-9}$	Rutherford et al. (1971)
R29	$\mathrm{Mg + NO^+ \rightarrow Mg^+ + NO}$	$k_{29} = 8.2\times10^{-10}$	Rutherford et al. (1971)
R30	$\mathrm{MgN_2{}^+ + O_2 \rightarrow MgO_2{}^+ + N_2}$	$k_{30} = 3.5\times10^{-12}$	Whalley et al. (2011)
R31	$\mathrm{MgO_2{}^+ + O \rightarrow MgO^+ + O_2}$	$k_{31} = 6.5\times10^{-10}$	Whalley and Plane (2010)
R32	$\mathrm{Mg^+ + H_2O + M \rightarrow MgH_2O^+ + M}$	$k_{32} = 2.3\times10^{-28}(T/200)^{-2.53}$	Martínez-Núñez et al. (2010)
R33	$\mathrm{Mg^+ + CO_2 + M \rightarrow MgCO_2{}^+ + M}$	$k_{33} = 4.6\times10^{-29}(T/200)^{-1.42}$	Whalley and Plane (2010)

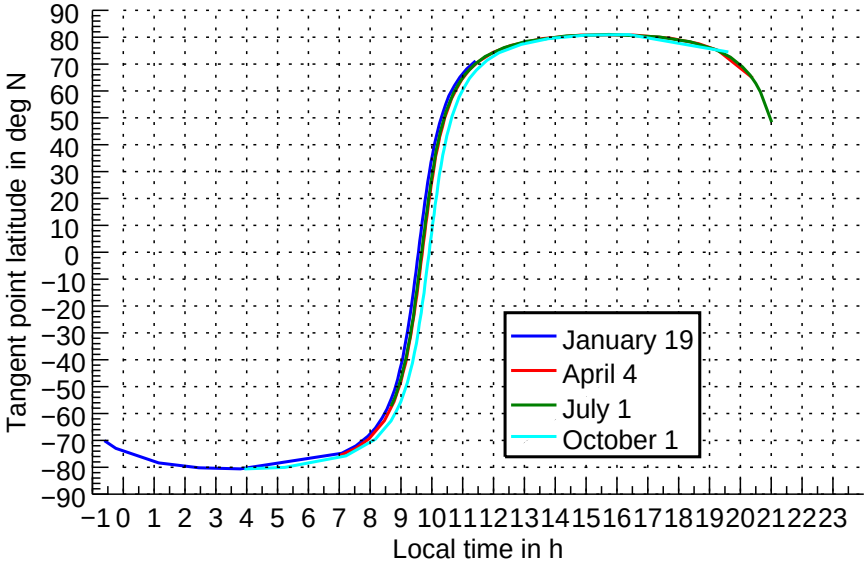

Fig. 1. Local time of SCIAMACHY measurements at different latitudes for different seasons of the year.

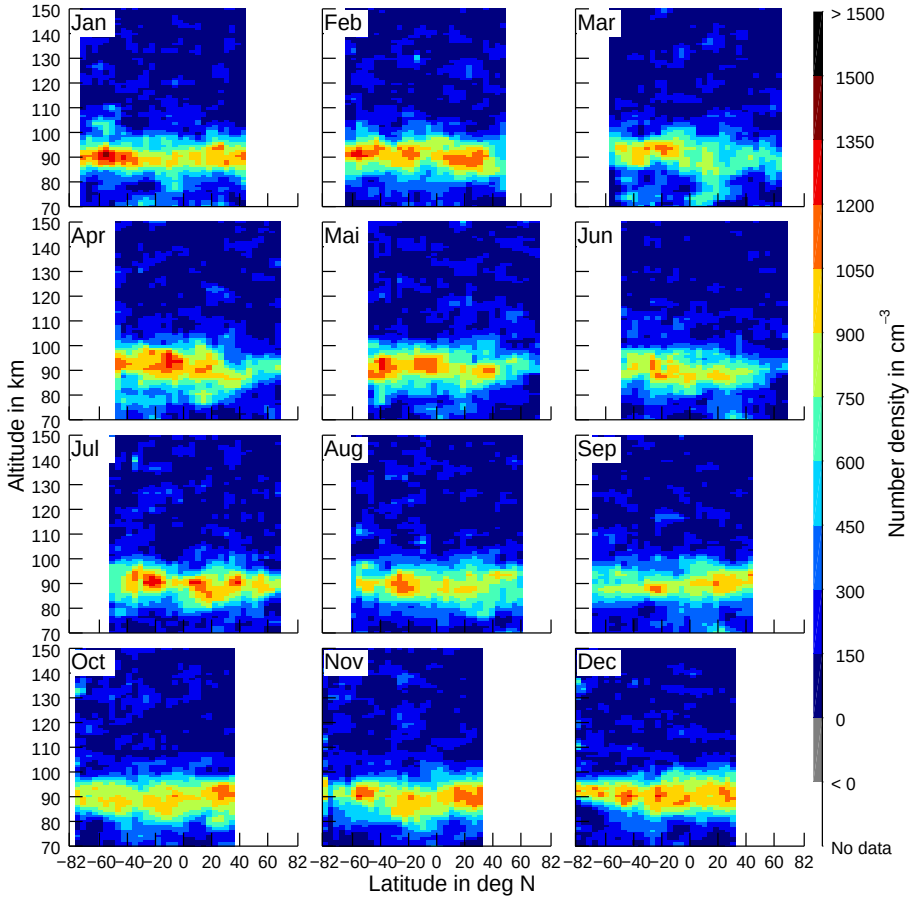

Fig. 2. Latitudinal variation of monthly (averaged over all January, February, etc. results from 2008–2012) and zonally averaged Mg density profiles retrieved from the 285.2 nm line. The Mg layer peaks around 90 km altitude and has a FWHM of about 15 km.

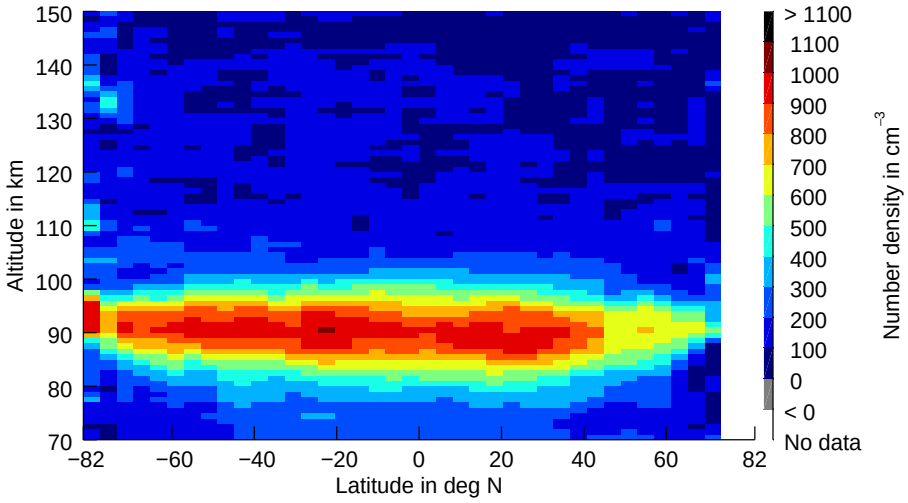

Fig. 3. Latitudinal variation of Mg profiles averaged over all available data for the years 2008–2012. Note that only between 45° N and S measurements from all 12 months contribute to the averages, while for high latitudes there is only summer coverage and/or near-terminator measurements.

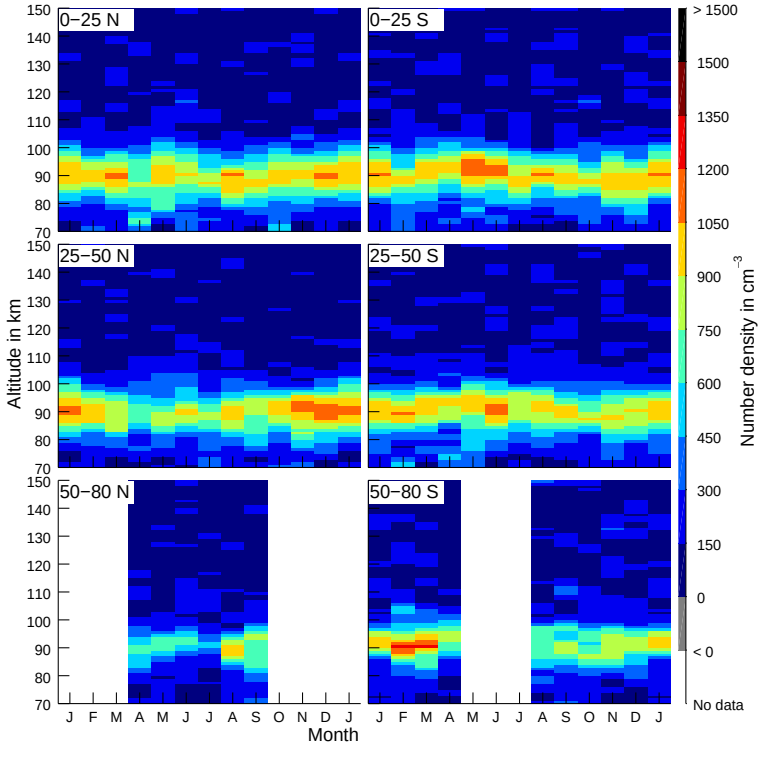

Fig. 4. Seasonal variation of the vertical Mg profile for different latitudinal zones (left: Northern Hemisphere (NH), right: Southern Hemisphere SH, top: low latitudes, mid: mid latitudes, bottom: high latitudes). The peak altitude is at 90 km for all latitudes with variations of ± 5 km. The month-to-month variations in peak altitude and density are bigger than any seasonal variations.

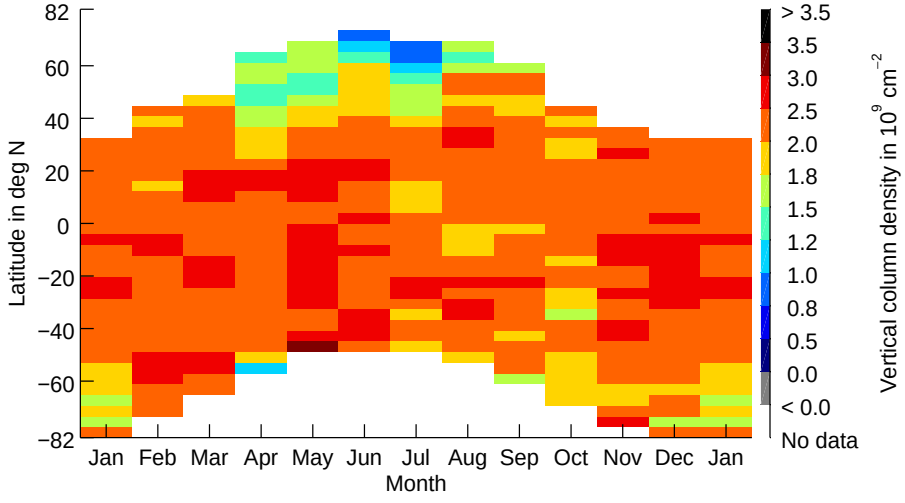

Fig. 5. Seasonal variation of the Mg vertical column density (VCD) between 70 km and 150 km for different latitudinal regions. The VCD varies between $0.5 \times 10^9\,\mathrm{cm}^{-2}$ and $3.5 \times 10^9\,\mathrm{cm}^{-2}$. No clear seasonal cycle is observed. Variations between consecutive days with measurements (at least 14 days difference) are even higher than the inter-monthly variations.

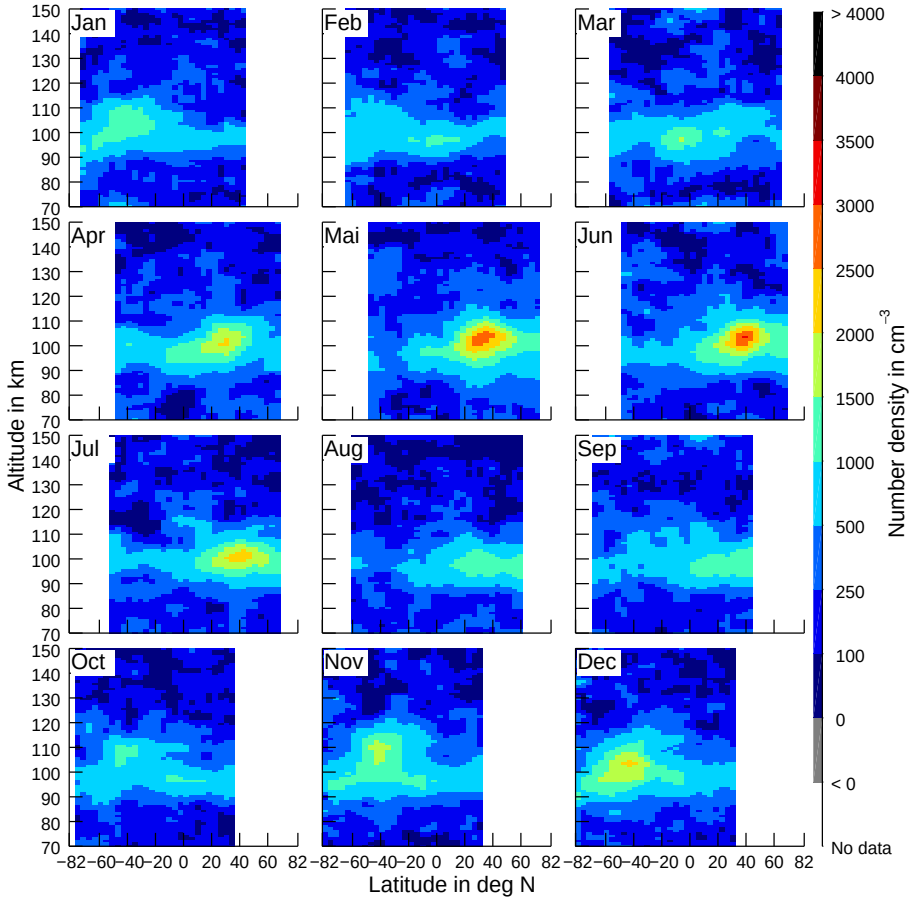

Fig. 6. Latitudinal variation of monthly and zonally averaged Mg^+ profiles (for the years 2008–2012) retrieved from the Mg^+ line at 280.4 nm. Mg^+ shows a seasonal cycle with a summer maximum, which is especially pronounced in the region between $25°$ and $45°$ latitude in the summer hemisphere. Furthermore, in this region the peak altitude is about 105 km, which is up to 10 km higher than at the equator or at the poles.

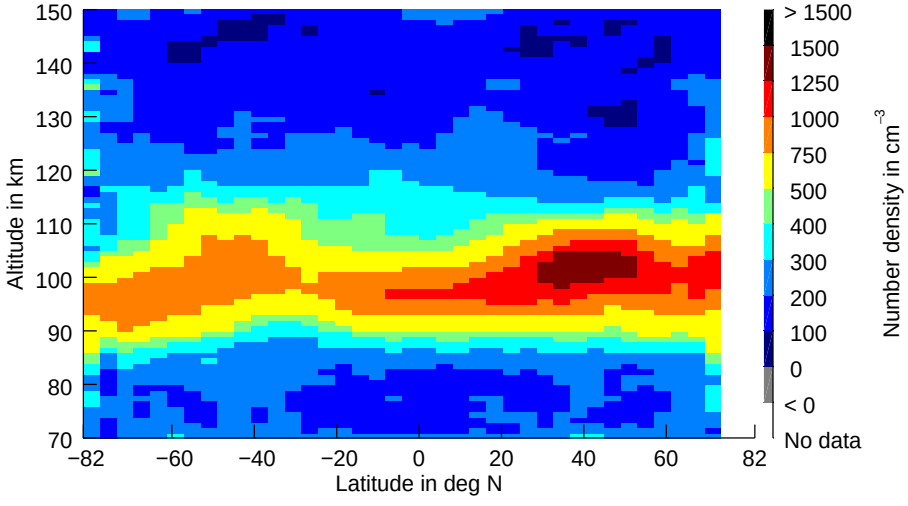

Fig. 7. Latitudinal variation of Mg^+ profiles averaged over all available data for 2008–2012 for the Mg^+ line at 280.4 nm.

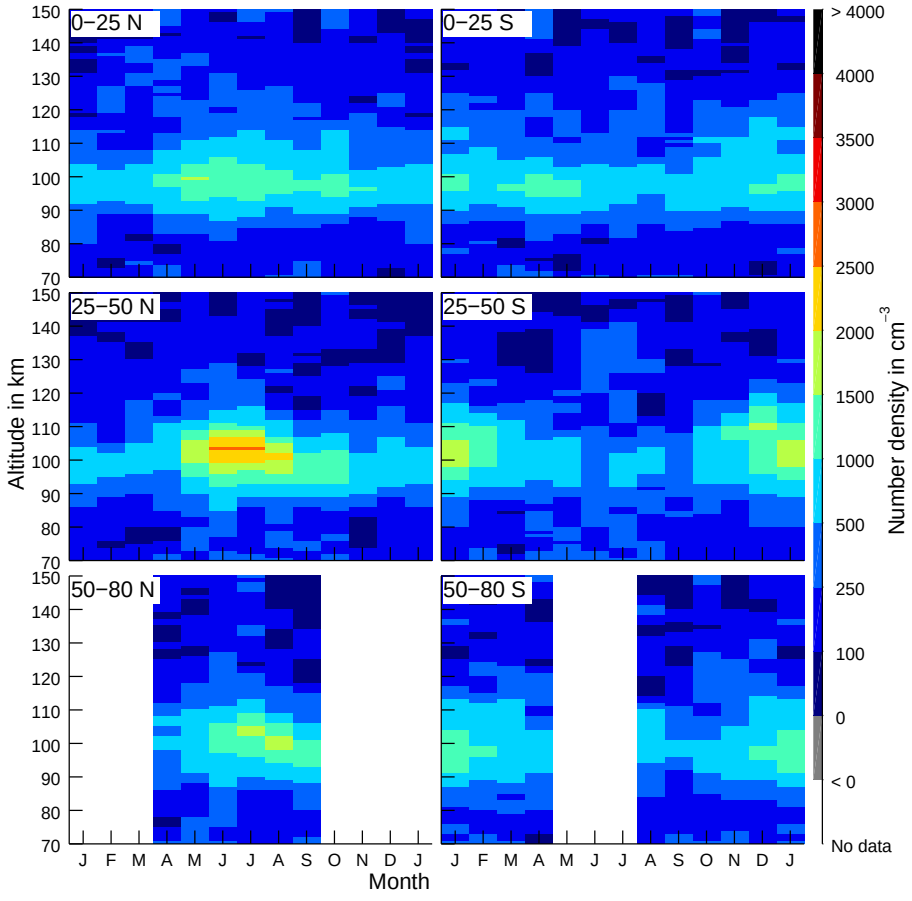

Fig. 8. Seasonal variation of the vertical profile of Mg^+ (280.4 nm line) for different latitudinal zones (left: NH, right: SH, top: low latitudes, mid: mid latitudes, bottom: high latitudes), averaged over all available observations in 2008–2012. For all these latitudinal zones a seasonal cycle in the peak altitude with a summer maximum and a winter minimum can be observed. The seasonal variations are similar or larger than the month-to-month variations. The maximum peak altitude is 5–10 km higher than the minimum peak altitude. For mid latitudes, the peak altitude in the winter hemisphere is still higher than the peak altitude at the equator (see also Fig. 6).

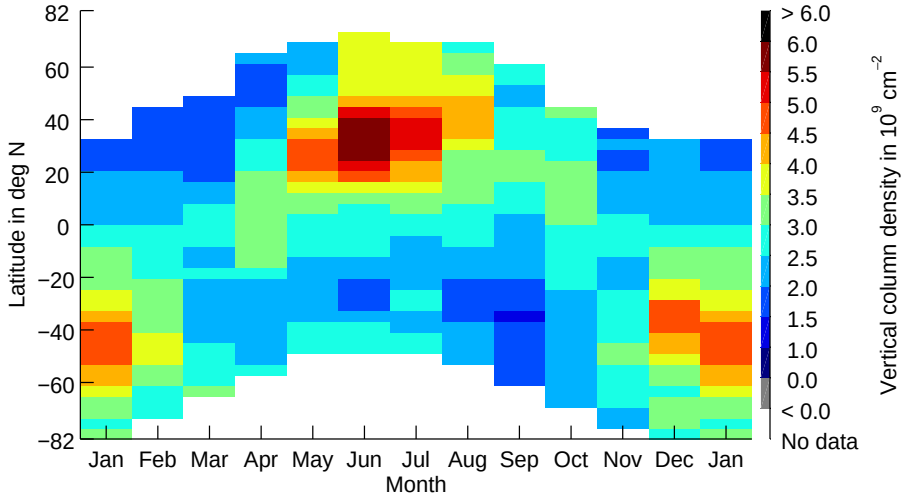

Fig. 9. Seasonal variation of the Mg^+ vertical column density (VCD) between $70\,\mathrm{km}$ and $150\,\mathrm{km}$ and for different latitudinal regions, retrieved from the $280.4\,\mathrm{nm}$ line. A clear seasonal cycle with a summer maximum can be observed. The summer maximum in the NH has higher values compared to the one in the SH. The highest variability can be found between $25°$ and $50°$ in both hemispheres.

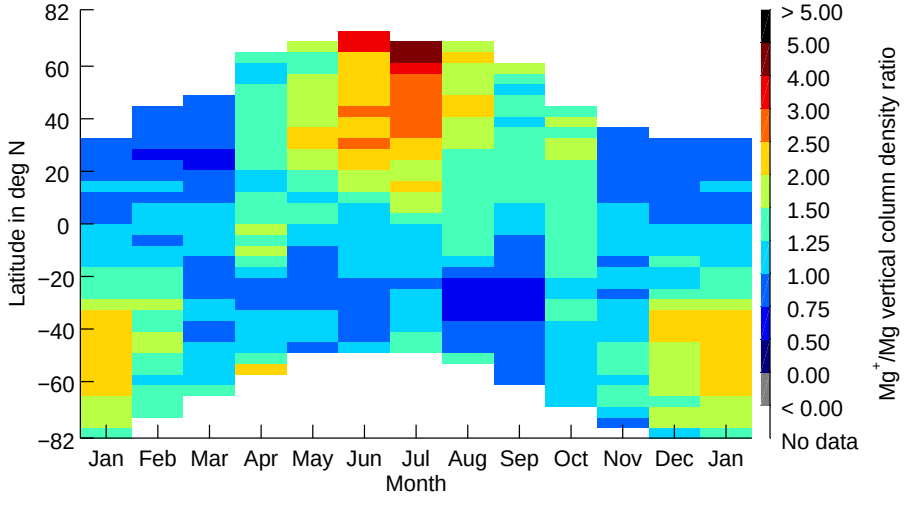

Fig. 10. Seasonal variation of the Mg^+ to Mg ratio for different latitudes. The ratio varies between 0.5 and 5 and shows a summer maximum, which is in good agreement with Correira et al. (2008).

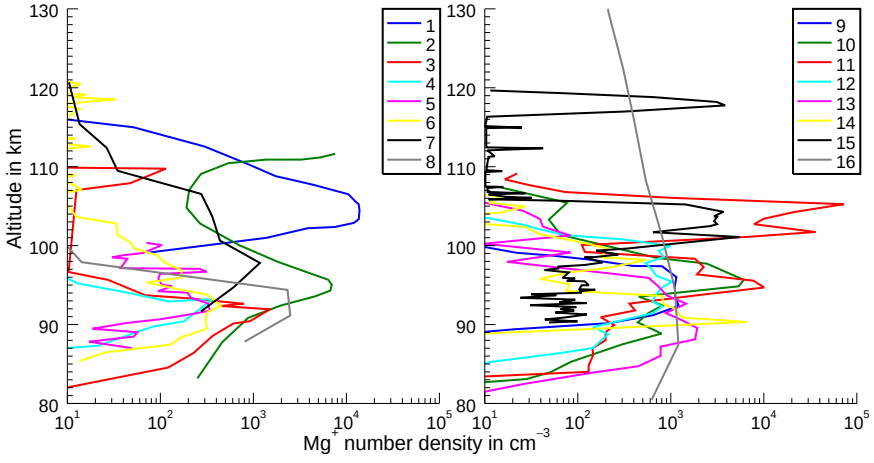

Fig. 11. Measurements of the vertical Mg^+ number density profile mentioned in the text and listed in table 1. Note, that the datapoints are redrawn from the original figures, and not all details of the original figures may be captured.

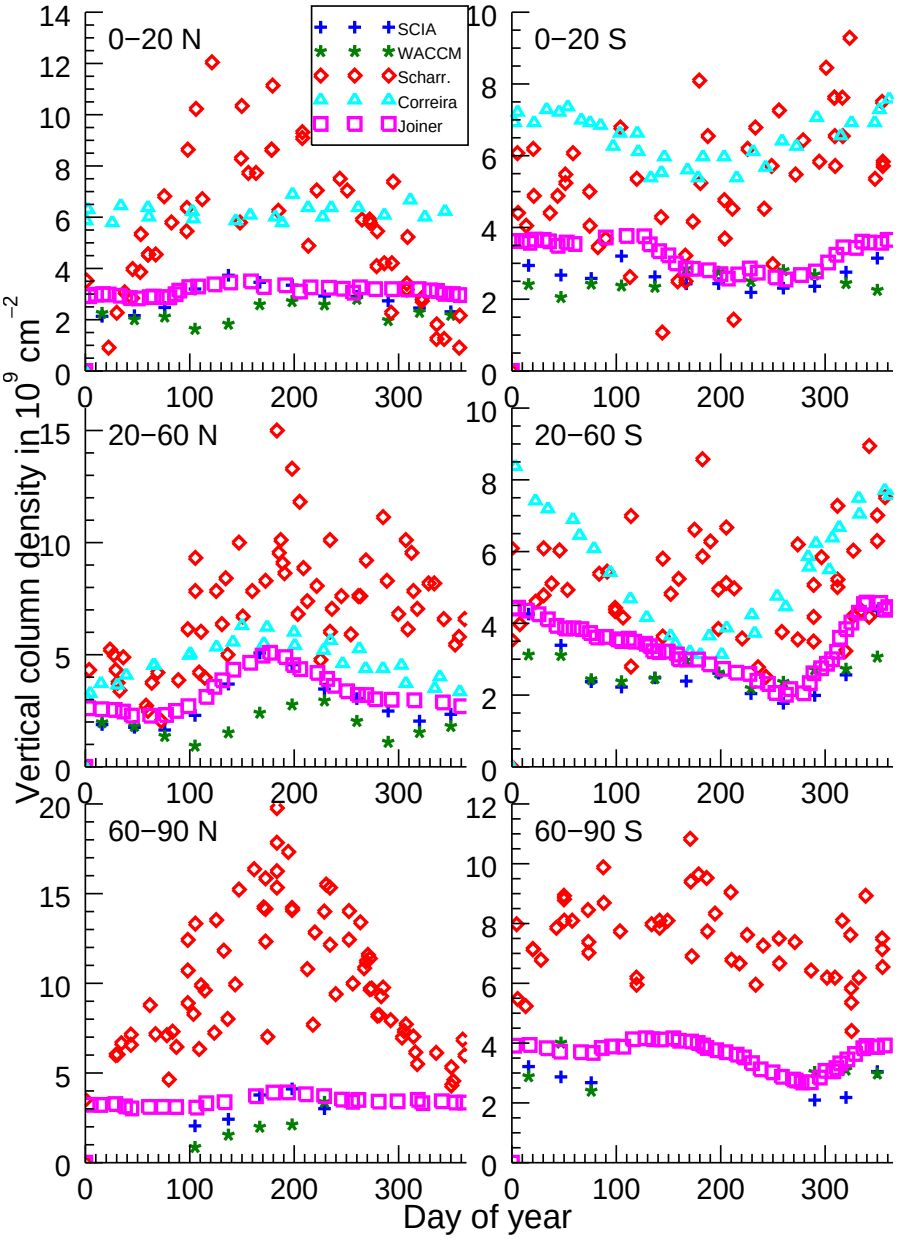

Fig. 12. Mg^+ VCD results for different latitudinal regions and from different sources. The left column shows the NH and the right column the SH. From top to bottom results for low, mid and high latitudes are shown. Note that different sources originally used different time periods. The data used is from SCIAMACHY (blue) and WACCM (green) from this work (0-20N/S, 20-60N/S, 60-90N/S, WACCM data co-located to SCIAMACHY coverage), from Scharringhausen (2007) (Figs. 7.3 and 7.4, red), from Correira et al. (2008) (Fig. 1, cyan) and Joiner and Aikin (1996) (Figs. 10 and 11, magenta).

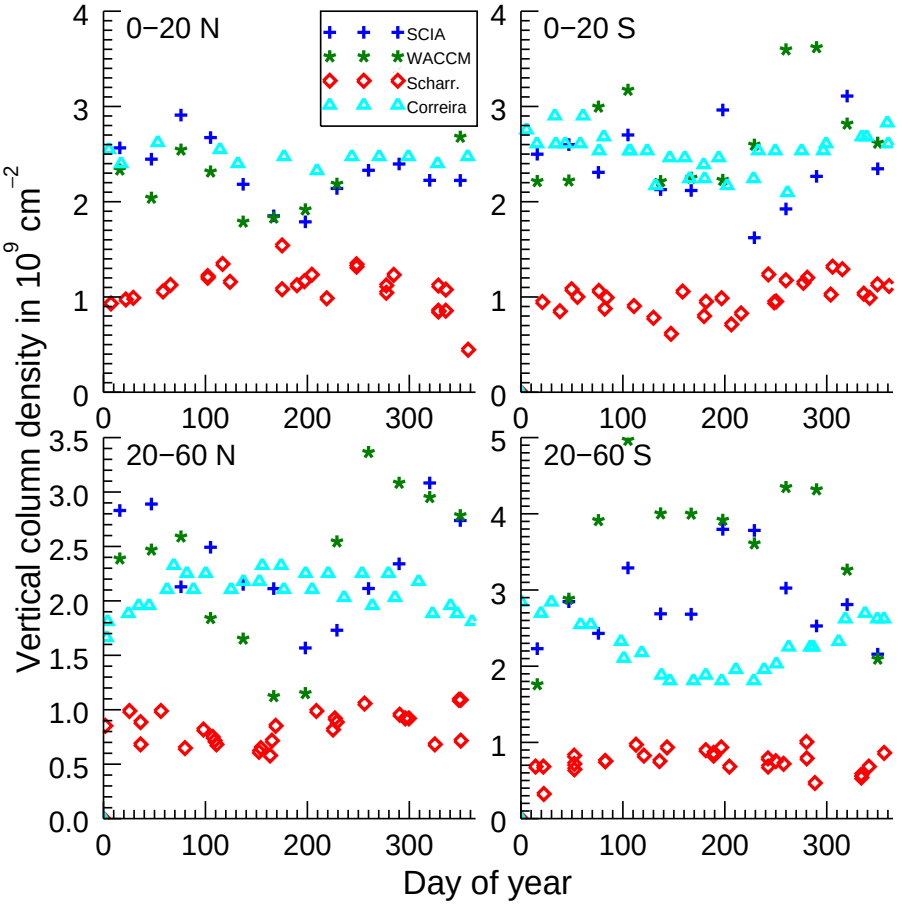

Fig. 13. Mg VCD results for different latitudinal regions and from different sources. The left column shows the NH and the right column the SH. From top to bottom results for low, mid and high latitudes are shown. Note that different sources originally used different time periods. The data used is from SCIAMACHY (blue) and WACCM (green) from this work (0-20N/S, 20-60N/S, 60-90N/S, WACCM data co-located to SCIAMACHY coverage), from Scharringhausen (2007) (Figs. 7.3 and 7.4, red) and from Correira et al. (2008) (Fig. 1, cyan).

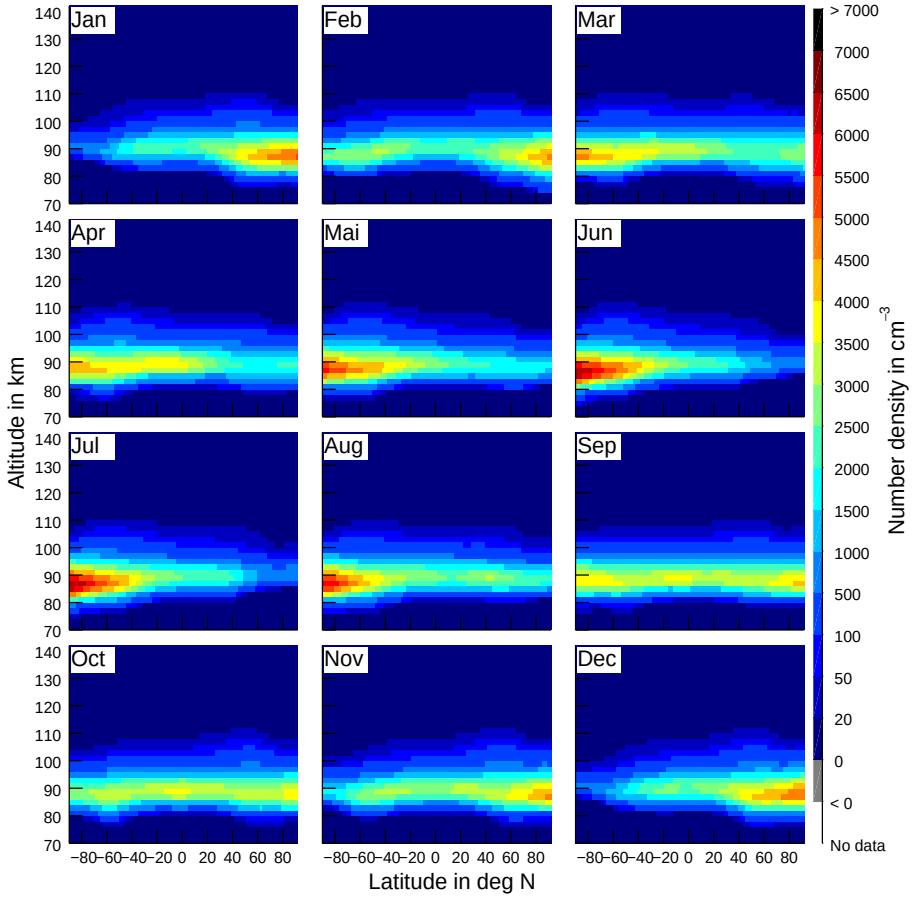

Fig. 14. Monthly mean WACCM results for Mg averaged over 7 yr from 2005 to 2011. The model results show a clear seasonal cycle with a winter maximum, most pronounced at high latitudes.

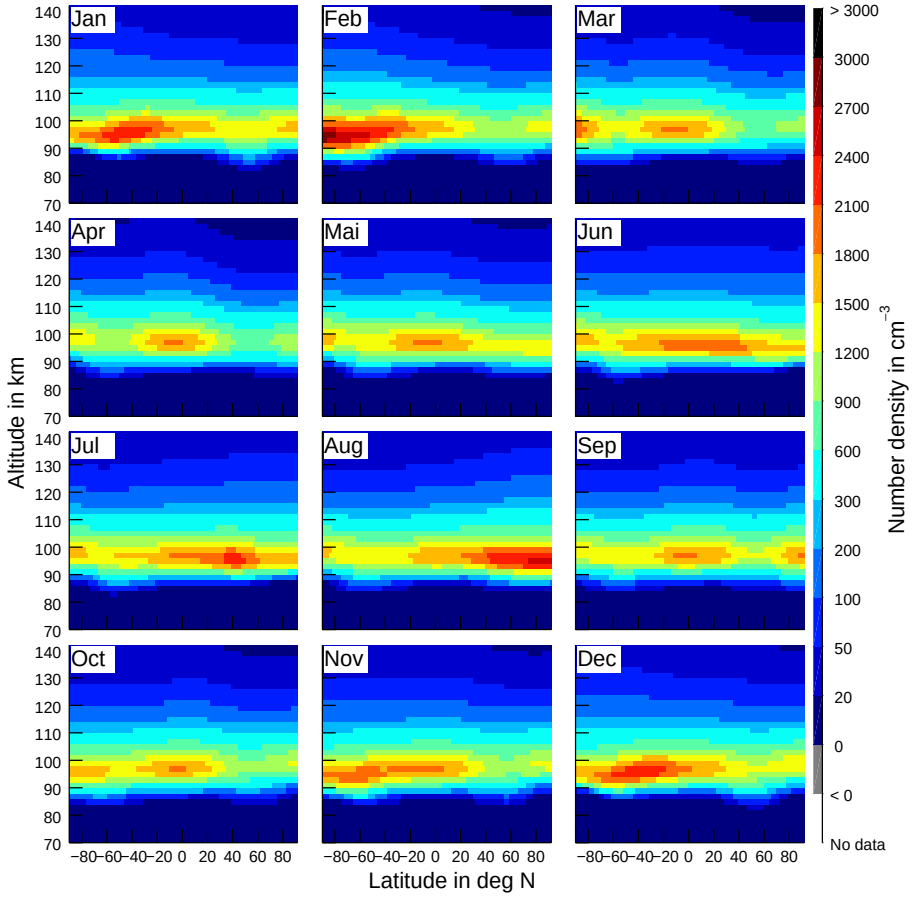

Fig. 15. Monthly mean WACCM results for Mg^+ averaged over 7 yr from 2005 to 2011. The model results show a clear seasonal cycle with a summer maximum, most pronounced at high latitudes. There is also a second smaller maximum at high latitudes for the winter hemisphere.

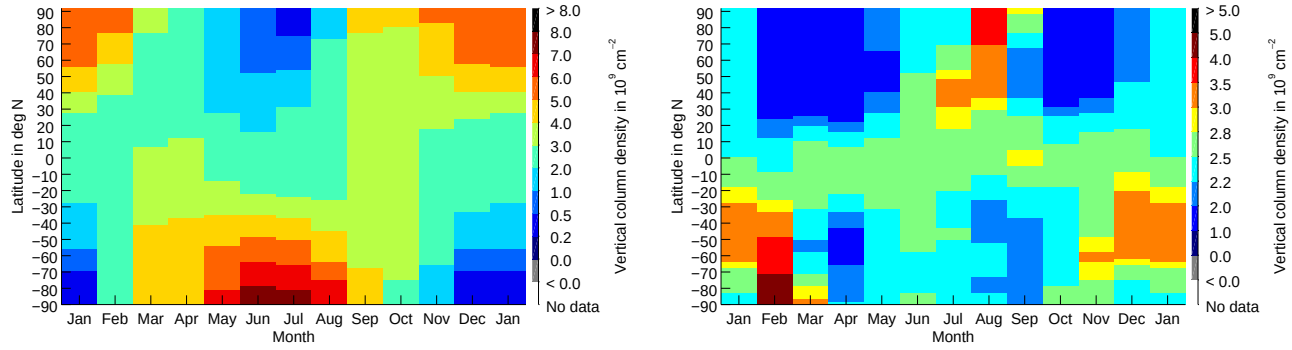

Fig. 16. WACCM VCD timelines for different latitudes for Mg (left) and Mg^+ (right). Mg VCD vary between $0.5 \times 10^9\,\mathrm{cm}^{-2}$ and $8 \times 10^9\,\mathrm{cm}^{-2}$ and show a clear seasonal cycle with a winter maximum, which is most pronounced at the poles. Mg^+ VCD vary from $1 \times 10^9\,\mathrm{cm}^{-2}$ to $5 \times 10^9\,\mathrm{cm}^{-2}$, with most VCD between $2 \times 10^9\,\mathrm{cm}^{-2}$ and $3 \times 10^9\,\mathrm{cm}^{-2}$. A clear seasonal cycle with a summer maximum for Mg^+ is observed. SCIAMACHY results of VCD are shown in Figs. 5 and 9.

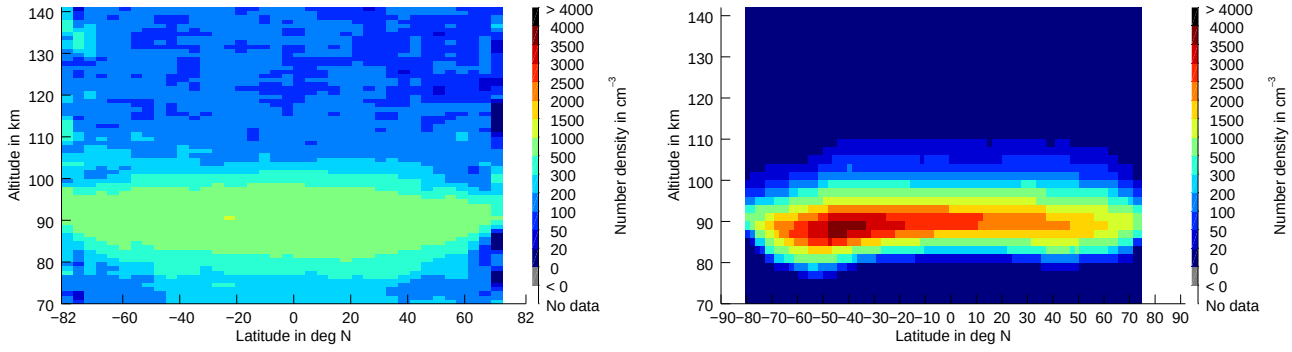

Fig. 17. Annual means of Mg for SCIAMACHY (left) and WACCM (right). SCIAMACHY measures smaller densities having a wider vertical profile than those of WACCM. The averaging for WACCM simulations is restricted to match the time periods, where SCIAMACHY measurements are available.

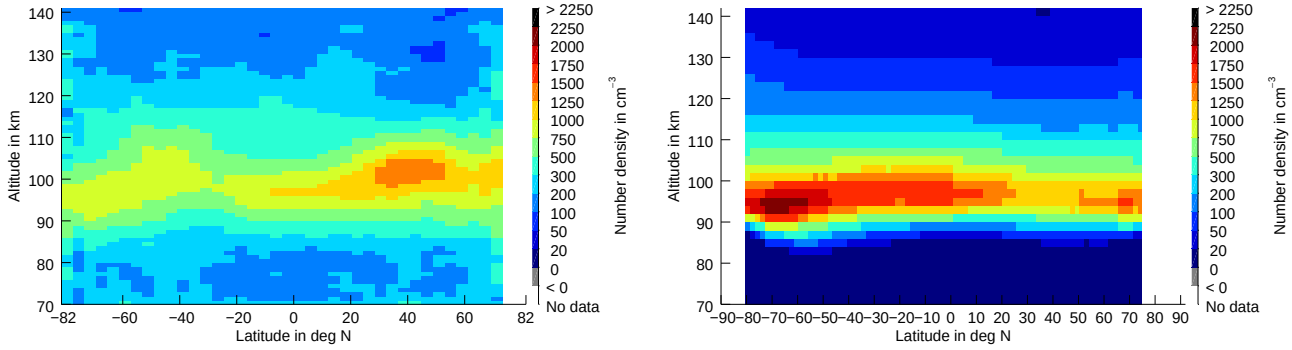

Fig. 18. Annual means of Mg^+ for SCIAMACHY (left, 280.4 nm) and WACCM (right). SCIAMACHY shows a wider vertical profile, and a stronger latitudinal dependence of the peak altitude. The peak densities are in very good agreement. The averaging for WACCM simulations is restricted to match the time periods, where SCIAMACHY measurements are available.

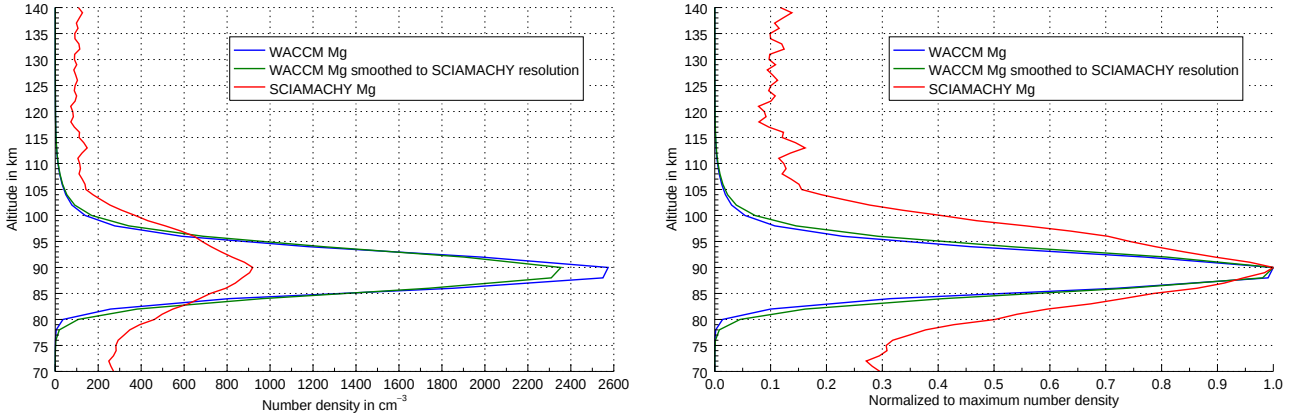

Fig. 19. Equatorial annual mean vertical profile of Mg for SCIAMACHY and WACCM. The right plot shows the profiles normalized to the maximum of each profile, to better compare the shape of the profiles. The smoothed profile is smoothed with a triangular function with a base width of 4 km. The VCD between 70 and 140 km is $2.3 \times 10^9\,\mathrm{cm}^{-2}$ for SCIAMACHY and $2.5 \times 10^9\,\mathrm{cm}^{-2}$ for WACCM. Note that the statistical error for SCIAMACHY estimated by Langowski et al. (2013) (Fig. 21) is $\approx \pm 200\,\mathrm{cm}^{-3}$ for the low density region above 100 km and below 80 km and $\approx \pm 400\,\mathrm{cm}^{-3}$ at 90 km.

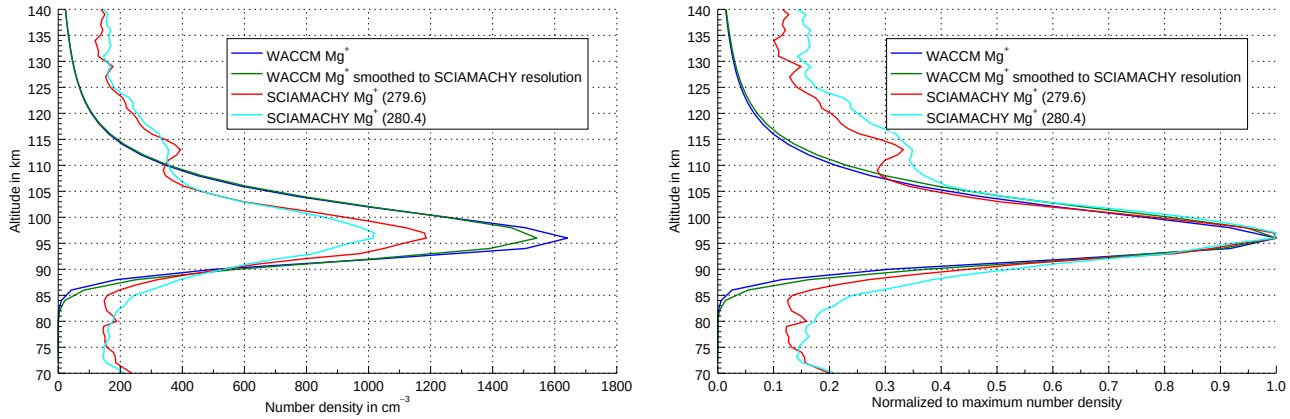

Fig. 20. Vertical profiles of Mg^+ for SCIAMACHY and WACCM at the equator. The right plot shows the profiles normalized to the maximum of each profile, to better compare the shape of the profiles. The VCD between 70 and 140 km at the equator is $2.7 \times 10^9\,\mathrm{cm}^{-2}$for SCIAMACHY (both 279.6 nm and 280.4 nm) and $2.4 \times 10^9\,\mathrm{cm}^{-2}$ for WACCM. Note that the statistical error for SCIAMACHY estimated by Langowski et al. (2013) (Figs. 22 and 23) is $\approx \pm 150\,\mathrm{cm}^{-3}$ for the 279.6 nm line and $\approx \pm 250\,\mathrm{cm}^{-3}$ for the 280.4 nm line.

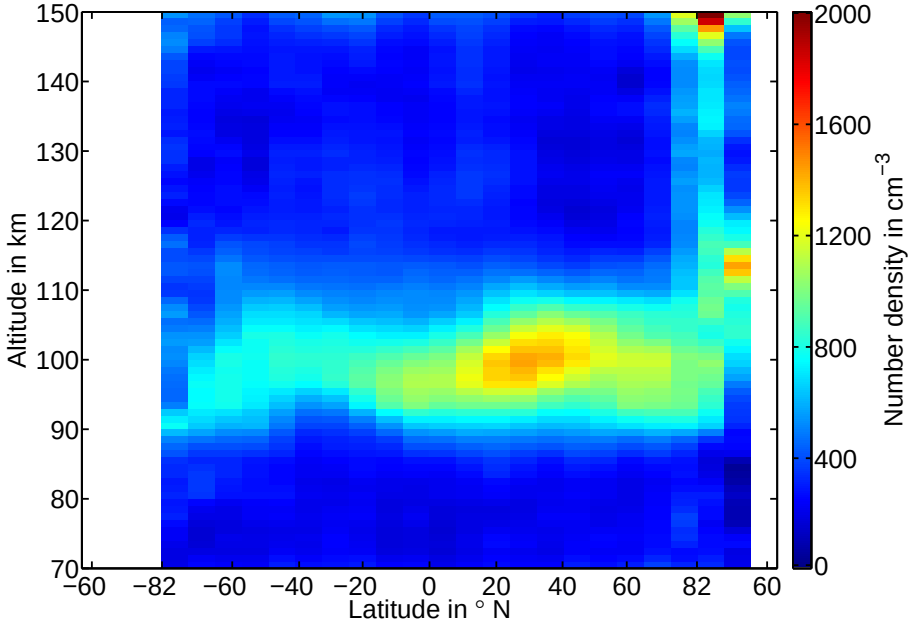

Fig. 21. Mg^+ profiles averaged over all available data for 2008–2012 for the Mg^+ line at 280.4 nm. The stray-light contaminated measurements at the start of the sunlit part of each orbit are also used here extending the coverage to higher northern latitudes and even the ascending node side. High Mg^+ densities are observed at the north pole. See Fig. 1 and Sect. 4 2nd paragraph for an explanation of the x-axis labels. Note that this is an older plot, which shows data with a wrong polarization correction, which is, however, unimportant for the effect shown here.

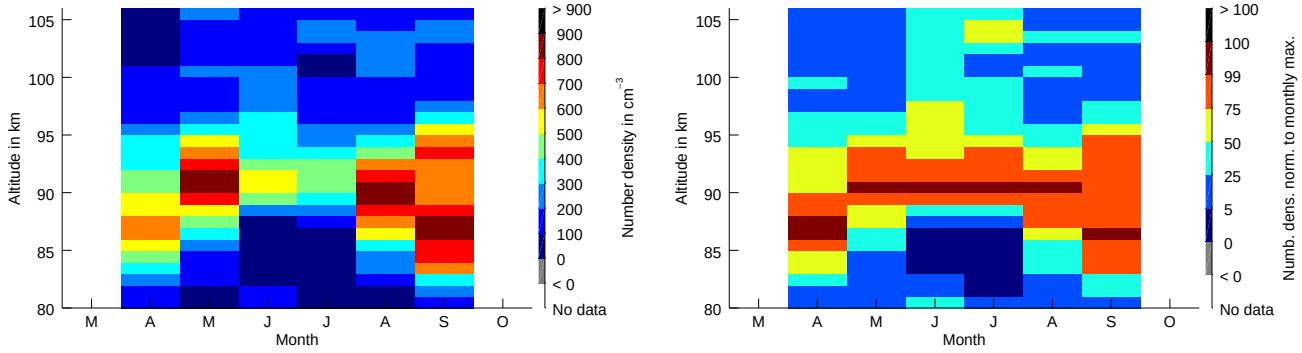

Fig. 22. Vertical profile of Mg densities (left) and Mg densities normalized to the monthly maximum (right) at 70°N, a latitude observed with SCIAMACHY. NLC occur at this latitude between about the end of May and mid-August.

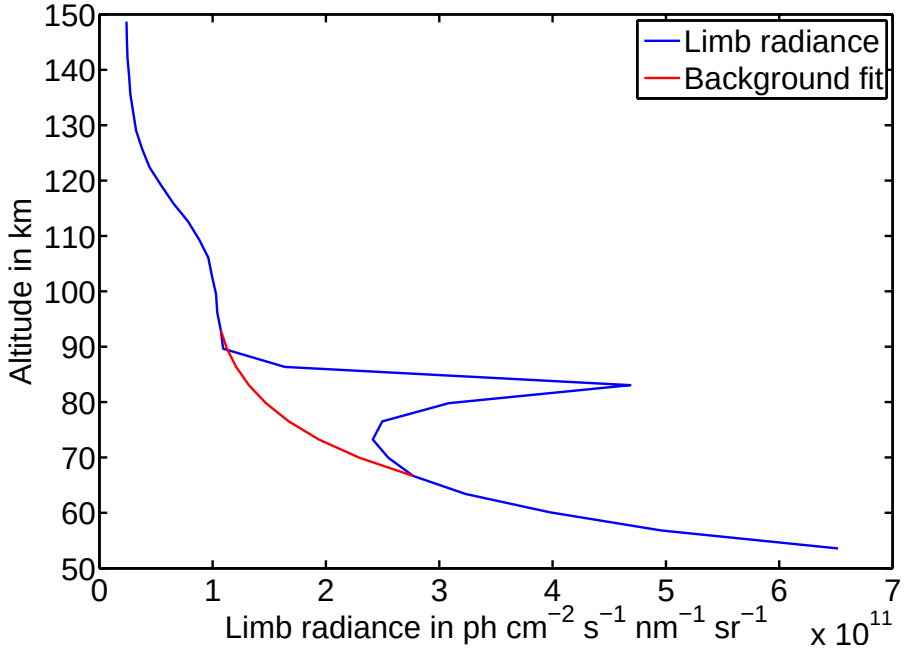

Fig. 23. Averaged SCIAMACHY limb MLT signal between 458 and 552 nm showing a NLC signature at 84 km and a background fit. The NLC radiance is quantified as the summed up differences between the signal and the background fit in the vicinity of the NLC signal.

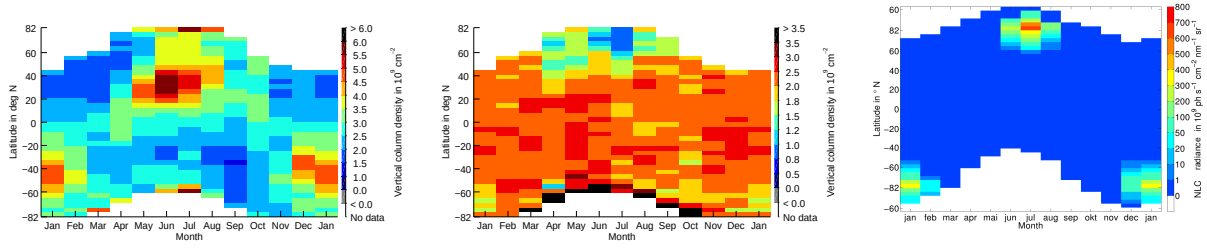

Fig. 24. Vertical column densities of Mg^+ (left), Mg (mid) and NLC radiance (right) retrieved from SCIAMACHY. A clear reduction of Mg^+ and Mg VCD is observed in the vicinity of NLC. However, this is also observed in neighbouring regions without NLC and can also be explained by other processes. (Note that the NLC retrieval includes more latitudes from the ascending node side).